Black hole sensitivities in Einstein-scalar-Gauss-Bonnet gravity

Félix-Louis Julié,[1,2] Hector O. Silva,[1,3] Emanuele Berti,[2] and Nicolás Yunes[3]

[1]*Max Planck Institute for Gravitational Physics (Albert Einstein Institute), Am Mühlenberg 1, 14476 Potsdam, Germany*

[2]*Department of Physics and Astronomy, Johns Hopkins University, 3400 North Charles Street, Baltimore, Maryland 21218, USA*

[3]*Illinois Center for Advanced Studies of the Universe, Department of Physics, University of Illinois at Urbana-Champaign, Urbana, Illinois 61801, USA*

(Received 21 February 2022; accepted 16 May 2022; published 16 June 2022)

The post-Newtonian dynamics of black hole binaries in Einstein-scalar-Gauss-Bonnet theories of gravity depends on the so-called "sensitivities"; quantities which characterize a black hole's adiabatic response to the time-dependent scalar field environment sourced by its companion. In this work, we calculate numerically the sensitivities of nonrotating black holes, including spontaneously scalarized ones, in three classes of Einstein-scalar-Gauss-Bonnet gravity: the shift-symmetric, dilatonic, and Gaussian theories. When possible, we compare our results against perturbative analytical results, finding excellent agreement. Unlike their general relativistic counterparts, black holes in Einstein-scalar-Gauss-Bonnet gravity only exist in a restricted parameter space controlled by the theory's coupling constant. A preliminary study of the role played by the sensitivities in black hole binaries suggests that, in principle, black holes can be driven outside of their domain of existence during the inspiral, for binary parameters which we determine.

DOI: 10.1103/PhysRevD.105.124031

I. INTRODUCTION

The detection of gravitational waves from compact binary coalescences by the LIGO-Virgo Collaboration [1–3] started a new era in experimental gravitational physics where, for the first time, we can test the predictions of general relativity (and modifications thereof) in highly-dynamical, nonlinear environments [4–12]. A prerequisite to perform such tests is a description of the orbital dynamics and the associated gravitational wave emission of inspiralling compact objects (i.e., neutron stars and black holes) in relativistic gravity theories [13–15].

A well-motivated class of modifications to general relativity introduces a dynamical scalar field that couples nonminimally to the Gauss-Bonnet density. These Einstein-scalar-Gauss-Bonnet (ESGB) theories arise in the low-energy limit of heterotic string theory [16], and also from the dimensional reduction of higher-dimensional Lovelock theories [17]. They are a subclass of Horndeski gravity [18,19] and also arise from an effective field theory perspective [20,21]. Due to the coupling between the scalar field and the Gauss-Bonnet density, black holes in these theories can violate no-hair theorems [22–37] and exhibit spontaneous scalarization [38–42]. As a consequence, black holes are endowed with a monopole scalar charge, which can source dipolar scalar radiation in binary black hole systems [43,44]. This makes black hole binaries ideal systems to constrain (or to look for evidence in favor of) these theories with current [10–12] and future gravitational-wave observatories [45,46].

With this motivation, considerable effort has been placed in developing tools to model the dynamics of black hole binaries in ESGB gravity, including the prediction of gravitational waveforms, using both post-Newtonian (PN) [43,47–50] and numerical relativity [51–59] approaches, the latter accompanied by works studying the Cauchy problem in this theory [60–65]. The "skeletonization" of an analytical black hole solution in this theory [47] can be used to show that the two-body Lagrangian describing the dynamics of black hole binaries at first PN order requires the knowledge of the so-called "sensitivities", quantities which characterize the adiabatic changes (more precisely, at constant Wald entropy) in the black holes' masses and scalar charges induced by the slowly varying external scalar field sourced by their companion, as illustrated in Fig. 1. These sensitivities are the black hole counterparts of a similar concept introduced for neutron stars in scalar-tensor theories in [66–70]. They also arise in the two-body problem in Einstein-Maxwell-scalar [71–73] and in Lorentz-violating theories [74,75].

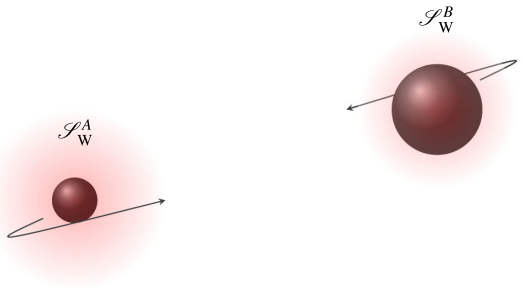

FIG. 1. Illustration of the problem. Two black holes with ADM masses $M_{A,B}$ and with scalar charges $Q_{A,B}$ are in a binary system. The scalar field of each black hole affects its companion, altering its mass and scalar charge. In the PN regime, and when finite-size corrections (e.g., tidal and out-of-equilibrium effects) can be neglected, these changes take place adiabatically, keeping the Wald entropy $\mathscr{S}^{A,B}_{\rm W}$ of each black hole constant. The change in the mass due to a slowly-varying scalar field environment at constant Wald entropy is the sensitivity, which we calculate here.

Here we develop a method to compute the sensitivities of nonrotating black holes using a full numerical approach. This requires, as a preliminary step, that we obtain black hole solutions that generalize those in the literature; we obtain families of constant Wald entropy black holes with nonvanishing asymptotic scalar fields. The sensitivities were also calculated using the analytical, but perturbative, approach of Ref. [47]. We show that the analytical Padé approximants obtained there (and extended to higher orders here) show remarkable agreement with numerical calculations. We also calculate, for the first time, the sensitivity of nonrotating, spontaneously scalarized black holes. With these results at hand, we speculate that black holes with real and regular scalar hair can cease to exist in binaries in ESGB theories, and we discuss the implications of this possibility. The method developed here to calculate the black hole sensitivity should be applicable in other gravitational theories as well.

The paper is organized as follows. In Sec. II we briefly review ESGB gravity and how black hole solutions are obtained numerically in this theory. In Sec. III we develop a strategy to calculate the sensitivities numerically, and present results for selected classes of ESGB theories. In Sec. IV we apply these results to study the evolution of black holes in binaries in this theory. Finally, in Sec. V we summarize our main findings and discuss possible avenues for future work. We use geometrical units ($G = c = 1$) throughout this work.

II. EINSTEIN-SCALAR-GAUSS-BONNET GRAVITY

A. Action and field equations

The theory we consider is described by the action

$$S = \frac{1}{16\pi}\int \mathrm{d}^4x\sqrt{-g}[R - 2(\partial\varphi)^2 + \ell^2 f(\varphi)\mathcal{G}], \quad (1)$$

where we use the same notation as in Ref. [47]: R is the Ricci scalar, $g = \det g_{\mu\nu}$ is the metric determinant, and φ a scalar field with kinetic term $(\partial\varphi)^2 = g^{\mu\nu}\partial_\mu\varphi\partial_\nu\varphi$ which couples to the Gauss-Bonnet invariant

$$\mathcal{G} = R^{\mu\nu\rho\sigma}R_{\mu\nu\rho\sigma} - 4R^{\mu\nu}R_{\mu\nu} + R^2 = R^{\mu\nu\rho\sigma}P_{\mu\nu\rho\sigma}, \quad (2)$$

where $R^\mu{}_{\nu\rho\sigma}$ and $R_{\mu\nu}$ are the Riemann and Ricci tensors, respectively, and

$$P^{\mu\nu}{}_{\rho\sigma} = R^{\mu\nu}{}_{\rho\sigma} - 2\delta^\mu{}_{[\rho}R^\nu{}_{\sigma]} + 2\delta^\nu{}_{[\rho}R^\mu{}_{\sigma]} + \delta^\mu{}_{[\rho}\delta^\nu{}_{\sigma]}R, \quad (3)$$

with brackets denoting antisymmetrization, as in $\delta^\mu{}_{[\rho}\delta^\nu{}_{\sigma]} = (1/2)(\delta^\mu{}_\rho\delta^\nu{}_\sigma - \delta^\mu{}_\sigma\delta^\nu{}_\rho)$. The tensor $P_{\mu\nu\rho\sigma}$ has the symmetries of the Riemann tensor and is divergence-free due to the Bianchi identities (see e.g., Refs. [63,76,77]). The integral of the Gauss-Bonnet scalar over a four-dimensional spacetime $\int \mathrm{d}^4x\sqrt{-g}\mathcal{G}$ is a boundary term [78]. The function $f(\varphi)$ defines the theory, and the Gauss-Bonnet coupling strength is set by the constant ℓ, with dimensions of length.

The field equations of the theory, obtained by varying the action (1) with respect to $g_{\mu\nu}$ and φ, are

$$R_{\mu\nu} = 2\partial_\mu\varphi\partial_\nu\varphi - 4\ell^2\left(P_{\mu\alpha\nu\beta} - \frac{1}{2}g_{\mu\nu}P_{\alpha\beta}\right)\nabla^\alpha\nabla^\beta f, \quad (4a)$$

$$\Box\varphi = -(\ell^2/4)f_{,\varphi}(\varphi)\mathcal{G}, \quad (4b)$$

where $P_{\mu\nu} = P^\alpha{}_{\mu\alpha\nu}$, ∇_μ is the metric-compatible covariant derivative associated to $g_{\mu\nu}$, and $\Box = \nabla^\mu\nabla_\mu$. We also use $(\cdot)_{,\varphi} = \mathrm{d}(\cdot)/\mathrm{d}\varphi$ to indicate derivatives with respect to the scalar field φ.

B. Nonrotating black holes

We are interested in obtaining static, spherically symmetric black hole solutions. We consider a line element of the form [37],

$$\mathrm{d}s^2 = -N(r)\sigma^2(r)\mathrm{d}t^2 + N(r)^{-1}\mathrm{d}r^2 + r^2(\sin^2\theta\mathrm{d}\theta^2 + \mathrm{d}\phi^2), \quad (5)$$

in Schwarzschild-Droste coordinates $x^\mu = \{t, r, \theta, \phi\}$ and a scalar field $\varphi(r)$. We define

$$N(r) = 1 - 2m(r)/r, \quad (6)$$

where $m(r)$ is the Misner-Sharp mass [79] such that $m(r) \to M$ as $r \to \infty$, and M is the Arnowitt-Misner-Deser (ADM) mass of the spacetime. The Schwarzschild solution is recovered by setting $m(r) = M$ and $\sigma = 1$. The Gauss-Bonnet invariant $\mathcal{G}$ for this line element is

$$\mathcal{G}=\frac{4}{r^2}\left[N'^2+\frac{\sigma'}{\sigma}N'(5N-3)+N(N-1)\left(\frac{N''}{N}+\frac{2\sigma''}{\sigma}\right)\right], \quad (7)$$

from which we can recover the familiar result $\mathcal{G}=48M^2/r^6$ in the Schwarzschild limit.

For convenience, we introduce the dimensionless quantities

$$r_*=r/r_H, \quad \text{and} \quad \ell_*=\ell/r_H, \quad (8)$$

where for now r_H is an arbitrary length (in this paper, an asterisk subscript will always denote a quantity that has been made dimensionless by dividing by r_H). We can then use Eq. (5) in the field equations (4a)–(4b) to obtain a system of differential equations for N', σ', and φ'', where $(\cdot)'=\mathrm{d}(\cdot)/\mathrm{d}r_*$. The steps are as follows. First, the (tt)- and (rr)-components of Eq. (4a) provide a system of two equations, which we can solve for m' and σ' in terms only of N and first and second derivatives of φ. These are the first two equations we need. Second, from the $(\theta\theta)$ component of Eq. (4a), we solve for m''. Finally, we can use the equations obtained in the previous step to eliminate m', m'', and σ' from Eq. (4b). This is the third equation we need.

Explicitly, the system of equations we work with is

$$\frac{1-N-r_*N'}{2}\left[1+\frac{2\ell_*^2}{r_*}(1-3N)\varphi' f_{,\varphi}\right]-\frac{r_*^2}{2}N\varphi'^2-\ell_*^2(N-1)\left\{2N\varphi'^2 f_{,\varphi\varphi}+\left[(1-3N)\frac{\varphi'}{r_*}+2N\varphi''\right]f_{,\varphi}\right\}=0, \quad (9a)$$

$$\frac{\sigma'}{\sigma}\left[1+\frac{2\ell_*^2}{r_*}(1-3N)\varphi' f_{,\varphi}\right]-\left[r_*\varphi'^2-\frac{2\ell_*^2}{r_*}(N-1)(\varphi'^2 f_{,\varphi\varphi}+\varphi'' f_{,\varphi})\right]=0, \quad (9b)$$

$$\begin{aligned}
&\varphi''\left[1+\frac{2\ell_*^2}{r_*}(1-7N)\varphi' f_{,\varphi}-\frac{12\ell_*^4}{r_*^4}[(N-1)^2+2r_*^2(1-3N)N\varphi'^2]f_{,\varphi}{}^2\right.\\
&\left.+\frac{8\ell_*^6}{r_*^5}\{6(N-1)^2+[1+3(2-5N)N]r_*^2\varphi'^2\}N\varphi' f_{,\varphi}{}^3\right]\\
&+\ell_*^2\left\{\frac{f_{,\varphi}}{r_*^4N}[3(1-N)^2+2r_*^2(1-N-12N^2)\varphi'^2-Nr_*^4\varphi'^4]-\frac{2}{r_*}(1-N)\varphi'^3 f_{,\varphi\varphi}\right\}\\
&+\frac{4\ell_*^4}{r_*^5}\{[-3(N-1)^2+2r_*^2(-1+3N)(-1+7N)\varphi'^2+Nr_*^4\varphi'^4]f_{,\varphi}\\
&-r_*(-1+N)[3(-1+N)+r_*^2(-1+3N)\varphi'^2]\varphi' f_{,\varphi\varphi}\}\varphi' f_{,\varphi}\\
&\times\frac{8\ell_*^6}{r_*^5}[r_*(1-3N)^2(1-5N)\varphi' f_{,\varphi}+3N(N-1)^2(2+r_*^2\varphi'^2)f_{,\varphi\varphi}]\varphi'^3 f_{,\varphi}{}^2+\frac{1+N}{r_*N}\varphi'=0. \quad (9c)
\end{aligned}$$

This is a system of three coupled ordinary differential equations for N', σ', and φ'', which then requires four initial conditions. The system can be solved numerically once a particular function f and value of ℓ_* have been chosen. For example, choosing $f=2\varphi$, we recover Eqs. (3.3)–(3.4) from Ref. [37] (see also [26]).

To obtain black hole solutions, we now identify r_H with the horizon radius and assume that the functions N, σ, and φ admit power series expansions near $r_*=1$ as

$$N=N_1^H(r_*-1)+\ldots, \quad (10a)$$

$$\sigma=\sigma_H+\sigma_1^H(r_*-1)+\ldots, \quad (10b)$$

$$\varphi=\varphi_H+\varphi_1^H(r_*-1)+\ldots. \quad (10c)$$

We can substitute these expressions into Eqs. (9) and solve order-by-order to fix all their coefficients in terms of ℓ_*, φ_H and σ_H only. In particular, we find

$$\varphi_1^H=-\frac{1-\sqrt{1-24\ell_*^4 f_{,\varphi}(\varphi_H)^2}}{4\ell_*^2 f_{,\varphi}(\varphi_H)}, \quad (11)$$

from which we conclude that ℓ_* and φ_H must satisfy the well-known condition [32]

$$24\ell_*^4 f_{,\varphi}(\varphi_H)^2<1, \quad (12)$$

for φ' to be real at the horizon, hence restricting the range of allowed values of φ_H given $\ell_*=\ell/r_H$.

We numerically integrate Eqs. (9) to find $N(r_*)$, $\sigma(r_*)$ and $\varphi(r_*)$ given four initial conditions on the horizon,

$$N = 0, \qquad \sigma = \sigma_H, \qquad \varphi = \varphi_H, \quad \text{and} \quad \varphi' = \varphi_1^H, \tag{13}$$

where φ_1^H is given by Eq. (11). Note that the numerical value of σ_H is pure gauge; it can always be absorbed in a rescaling of time t, cf. Eq. (5). Hence, black hole solutions depend on two integration constants only, φ_H and $\ell_* = \ell/r_H$. The latter fully takes into account the dependence on the fundamental coupling ℓ, which only enters through this ratio in Eqs. (9).

We can also expand N, σ, and φ in inverse powers of r_* to study their asymptotic behavior at spatial infinity, i.e., for $r_* \gg 1$. By substituting the series

$$N = 1 - \frac{2M_*}{r_*} + \frac{N_2^\infty}{r_*^2} + \frac{N_3^\infty}{r_*^3} + \ldots, \tag{14a}$$

$$\sigma = 1 + \frac{\sigma_1^\infty}{r_*} + \frac{\sigma_2^\infty}{r_*^2} + \frac{\sigma_3^\infty}{r_*^3} + \ldots, \tag{14b}$$

$$\varphi = \bar{\varphi} + \frac{Q_*}{r_*} + \frac{\varphi_2^\infty}{r_*^2} + \frac{\varphi_3^\infty}{r_*^3} + \ldots, \tag{14c}$$

into Eqs. (9) and solving iteratively we find

$$\begin{aligned} &N_2^\infty = Q_*^2, \qquad N_3^\infty = M_* Q_*^2, \\ &\sigma_1^\infty = 0, \qquad \sigma_2^\infty = -Q_*^2/2, \qquad \sigma_3^\infty = -4M_* Q_*^2/3, \\ &\varphi_2^\infty = M_* Q_*, \qquad \varphi_3^\infty = (8M_*^2 Q_* - Q_*^3)/6. \end{aligned} \tag{15}$$

At all orders, the coefficients entering Eq. (14) are functions of *three* constants M_*, Q_*, and $\bar{\varphi}$. For black holes, all three quantities are fixed by the *two* integration constants ℓ_* and φ_H [once σ_H is set to ensure the gauge $\sigma = 1$ at infinity as in Eq. (14b)]; the "scalar hair" is said to be "secondary" [80,81]. Although M_*, Q_*, and $\bar{\varphi}$ can be obtained from the $\mathcal{O}(r_*^{-1})$ falloff of N and φ, we also use subleading terms up to $\mathcal{O}(r_*^{-3})$ and the expansion of σ to accurately extract them from our numerical integration, which terminates at a finite r_*.

Let us conclude this section by further illustrating the consequences of Eq. (12), as it will play an important role below. Solving analytically for the coefficients of Eqs. (10) up to φ_4^H, N_4^H, and σ_3^H, we can compute the near-horizon scalar field and Gauss-Bonnet invariant (7) as

$$\varphi = \varphi_H + \sum_{n=1}^{4} \varphi_n^H (r_* - 1)^n + \mathcal{O}(r_* - 1)^5, \tag{16a}$$

$$\mathcal{G} r_H^4 = g_H + \sum_{n=1}^{2} g_n^H (r_* - 1)^n + \mathcal{O}(r_* - 1)^3, \tag{16b}$$

where φ_1^H is given by Eq. (11) and where the other coefficients are long functions of ℓ_* and φ_H [but not of the gauge-fixing quantity σ_H, see below Eq. (13)] available online [82]. However, near the saturation of the bound (12), i.e., when $\epsilon^2 = 1\text{–}24\ell_*^4 f_{,\varphi}(\varphi_H)^2 \ll 1$ but $\epsilon \neq 0$, we find

$$\varphi_1^H = -\sqrt{\frac{3}{2}} + \mathcal{O}(\epsilon), \tag{17a}$$

$$\varphi_2^H = \sqrt{\frac{3}{2}} \frac{9}{16} \frac{\chi}{\epsilon} + \mathcal{O}(\epsilon^0), \tag{17b}$$

$$\varphi_3^H = -\sqrt{\frac{3}{2}} \frac{27}{128} \frac{\chi^2}{\epsilon^3} + \mathcal{O}(\epsilon^{-2}), \tag{17c}$$

$$\varphi_4^H = \sqrt{\frac{3}{2}} \frac{729}{4096} \frac{\chi^3}{\epsilon^5} + \mathcal{O}(\epsilon^{-4}), \tag{17d}$$

and

$$g_H = 48 + \mathcal{O}(\epsilon), \tag{18a}$$

$$g_1^H = -216 \frac{\chi}{\epsilon} + \mathcal{O}(\epsilon^0), \tag{18b}$$

$$g_2^H = \frac{729}{4} \frac{\chi^2}{\epsilon^3} + \mathcal{O}(\epsilon^{-2}), \tag{18c}$$

with $\chi = 3 + 4\ell_*^2 f_{,\varphi\varphi}(\varphi_H)$. While φ_1^H and g_H are finite and do not depend on $f(\varphi)$ in this limit, every other coefficient in Eqs. (17)–(18) is singular. We find qualitatively similar results, that we report in Appendix A, for the Ricci and Kretschmann curvature invariants R and $\mathcal{K} = R^{\mu\nu\rho\sigma} R_{\mu\nu\rho\sigma}$. In Sec. III A, we will compare the analytic predictions (16) to numerical results.

III. BLACK HOLE SENSITIVITIES

The PN dynamics of black hole binaries in ESGB gravity was studied in Refs. [43,47–49] in the weak-field, slow-orbital velocity limit. In this context, Refs. [47,83] showed that when finite-size corrections (e.g., tidal and out-of-equilibrium effects) can be neglected, each black hole is described by a sequence of static configurations with identical Wald entropy $\mathcal{S}_{\rm W}$ defined as [84–86]

$$\mathcal{S}_{\rm W} = \frac{\mathcal{A}_H}{4} + 4\pi\ell^2 f(\varphi_H), \tag{19}$$

where $\mathcal{A}_H$ is the horizon surface area (here $4\pi r_H^2$). The PN Lagrangian [47] and fluxes [43,48,49] then depend on "sensitivities" which characterize the response of each black hole to its adiabatically changing scalar-field environment.

More precisely, the sensitivity of a black hole is defined as the logarithmic change in M with respect to $\bar{\varphi}$ [cf. Eq. (14c)] at *fixed Wald entropy* $\mathcal{S}_{\rm W}$ [47,83],

$$\alpha \equiv \left.\frac{\mathrm{d}\ln M}{\mathrm{d}\bar{\varphi}}\right|_{\mathscr{S}_{\mathrm{W}}} = \left.\frac{1}{M}\frac{\mathrm{d}M}{\mathrm{d}\bar{\varphi}}\right|_{\mathscr{S}_{\mathrm{W}}}, \tag{20}$$

and we denote its derivative with respect to $\bar{\varphi}$, which also enters the 1PN Lagrangian [47], by β,

$$\beta \equiv \left.\frac{\mathrm{d}\alpha}{\mathrm{d}\bar{\varphi}}\right|_{\mathscr{S}_{\mathrm{W}}}. \tag{21}$$

Equation (20) is similar to the notion of sensitivity for self-gravitating bodies (such as neutron stars) in scalar-tensor theories, defined as the logarithmic change in the ADM mass M with respect to some external $\bar{\varphi}$, but at fixed baryonic mass [68–70].

In a binary, the sensitivity α of a body accounts for the readjustments of its ADM mass M and scalar charge Q during the inspiral. This sensitivity has to be evaluated at a value $\bar{\varphi}$ corresponding to its time-varying but spatially homogeneous background scalar field sourced by the far-away companion (recall that finite-size effects are here neglected). For our purposes, we take $\bar{\varphi}$ to be just some nonzero scalar field value in which the isolated black hole is embedded.

Reference [47] also showed that the variation of $\mathscr{S}_{\mathrm{W}}$, M and $\bar{\varphi}$ with respect to the black hole's integration constants (here ℓ_* and φ_H, see Sec. II B) must satisfy the identity

$$T\delta\mathscr{S}_{\mathrm{W}} = \delta M + Q\delta\bar{\varphi}, \tag{22}$$

where T is the temperature [47], whose expression we do not need here. Comparing this first law of thermodynamics in the case of interest ($\delta\mathscr{S}_{\mathrm{W}} = 0$) with the definition (20) we get

$$\alpha = -Q/M, \tag{23}$$

which provides a second, independent way of calculating the black hole sensitivity.

We numerically calculate the sensitivity α as follows:

(1) Fix a value of the dimensionless ratio ℓ/μ, where

$$\mu^2 = \frac{\mathscr{S}_{\mathrm{W}}}{4\pi} \tag{24}$$

is the irreducible mass squared [87]. From Eq. (19), this ratio is related to $\ell_* = \ell/r_H$ and φ_H through

$$(\ell/\mu)^{-2} = (4\ell_*^2)^{-1} + f(\varphi_H). \tag{25}$$

(2) Choose a value of the scalar field at the horizon φ_H.

(3) Using Eq. (25), solve for ℓ_* and use this value to numerically construct a black hole, integrating the system (9) with initial conditions (13) at $r_* = 1$ up to a large value of r_*. The constant σ_H is pure gauge and we fix it by requiring that the line element (5) asymptotes to $\sigma = 1$.

(4) Calculate the quantities $\bar{\varphi}$, M_* and Q_* from the asymptotic expressions (14).

(5) Repeat steps (2) to (4) for the range of φ_H values allowed by Eq. (12), hence obtaining a family of constant Wald entropy black holes. For such a family the condition (12) becomes

$$\frac{3}{2}f_{,\varphi}(\varphi_H)^2 < [(\mu/\ell)^2 - f(\varphi_H)]^2. \tag{26}$$

(6) Since a constant $\mathscr{S}_{\mathrm{W}}$ is equivalent to a constant μ, we can calculate α numerically by inserting

$$M/\mu = M_*(\ell/\mu)\ell_*^{-1} \tag{27}$$

into Eq. (20), or by directly computing the scalar-charge-to-mass ratio $-Q_*/M_* = -Q/M$ [cf. Eq. (23)], which is invariant under rescaling by r_H. Once we know α, we calculate β using Eq. (21).

The numerical methods used in this paper are summarized in Appendix B. In calculations that will follow, we will be interested in the behavior of certain quantities close to the saturation of Eq. (26). Numerically, we can only reach a minimum value of $\epsilon = |\varphi_H - \varphi_H^{\max}|$, where $\varphi_H^{\max}$ saturates Eq. (26). Here we take $\epsilon \sim 10^{-5}$, and we will refer to the limiting process as "approaching the saturation of Eq. (26)".

In the context of PN calculations, M/μ, α, and β must be viewed as functions of the asymptotic scalar field $\bar{\varphi}$, the irreducible mass μ, and the fundamental constant ℓ. The last two only contribute through their dimensionless ratio ℓ/μ, since the only free parameter entering the differential equations (9) is ℓ_*, which is in turn related to ℓ/μ through Eq. (25). We find full agreement between both methods specified in step 6 above to compute the sensitivity α. This proves that our families of constant-entropy black holes are consistent with the first law of thermodynamics; see the discussion following Eq. (22).

When possible, our numerical results will be compared against the analytical black hole sensitivities obtained in a small-ℓ/μ expansion around Schwarzschild in Ref. [47]. The results there have the schematic form

$$\alpha = -\frac{x}{2} - \sum_{n=2}^{N} A_n(\bar{\varphi})x^n, \qquad x = \frac{\ell^2 f'(\bar{\varphi})}{\mu^2}, \tag{28}$$

where the coefficients A_n depend on f and its derivatives evaluated at $\bar{\varphi}$. The calculation in Ref. [47] obtained the series (28) up to $N = 4$ and here we extend it up to $N = 10$ for a more careful comparison with our numerical results. These lengthy results are available online [82].

In the following subsections we compare the numerical and analytical calculations for black holes for three particular choices of the coupling function f.

A. Shift-symmetric theory

As a first example, consider the theory

$$f(\varphi) = 2\varphi, \tag{29}$$

such that the action (1) becomes invariant under the shift $\varphi \to \varphi + \Delta\varphi$, where $\Delta\varphi$ is a constant. The condition for the existence of a real scalar field at the horizon of constant entropy black holes (26) simplifies to

$$\varphi_H < \frac{1}{2}\left(\frac{\mu^2}{\ell^2} - \sqrt{6}\right). \tag{30}$$

In Fig. 2, we show the radial profiles of the Gauss-Bonnet invariant (top panel) and scalar field (bottom panel),

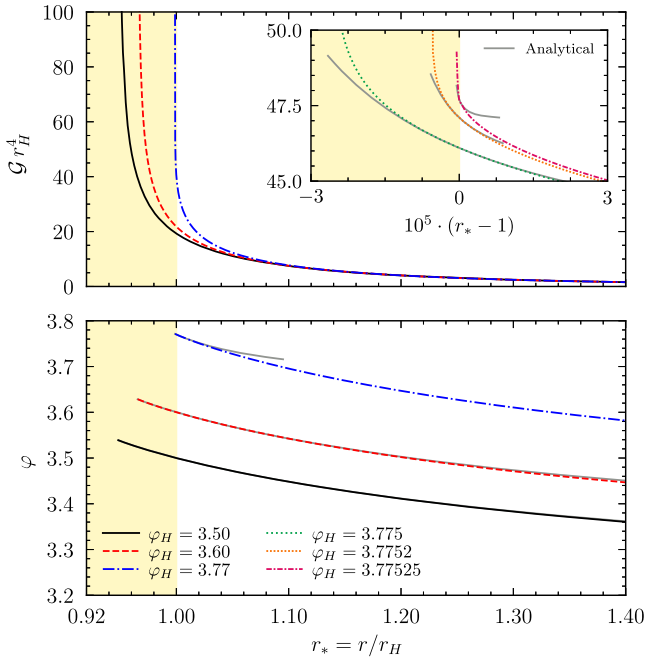

FIG. 2. A sequence of constant $(\ell/\mu)^2 = 10^{-1}$ black holes with φ_H approaching $\varphi_H^{\max} \approx 3.77526$, inside (shaded region, $r_* < 1$) and outside ($r_* > 1$) the horizon. Top panel: the Gauss-Bonnet scalar diverges at $r_* = \{0.956, 0.965, 0.999\}$ when $\varphi_H = \{3.50, 3.60, 3.77\}$ approaches $\varphi_H^{\max}$. The inset also shows $\varphi_H = \{3.775, 3.7752, 3.77525\}$, closing in into $\varphi_H^{\max}$ one order of magnitude after another. Bottom panel: the scalar field is finite at the curvature singularity. In the bottom panel and in the top panel's inset, the numerical results agree at $r_* = 1$ with the (2,2)-Padé resummation of Eq. (16a) and the (1,1)-Padé resummation of Eq. (16b), respectively. In particular, $\mathcal{G}r_H^4$ approaches the value 48 when φ_H approaches $\varphi_H^{\max}$, hence recovering Eq. (18a), with $\mathcal{G}r_H^4 \approx 47.73$ for $\varphi_H = 3.77525$. Both $\mathcal{G}r_H^4$ and φ converge to finite values for all $r_* \geq 1$ when φ_H is increased towards $\varphi_H^{\max}$.

both inside (shaded region, $r_* < 1$) and outside ($r_* > 1$) the horizon, for a sequence of constant $(\ell/\mu)^2 = 10^{-1}$ black holes, as φ_H approaches the maximum value $\varphi_H^{\max} = (10 - \sqrt{6})/2 \approx 3.77526$ saturating Eq. (30). As is well known from, e.g., Refs. [29,35], the black holes have a hidden curvature singularity which is driven towards the horizon as φ_H approaches $\varphi_H^{\max}$. However, in this paper we wish to shed new light on this phenomenon. To this aim, we carefully let φ_H approach $\varphi_H^{\max}$ one order of magnitude after another, since we cannot saturate Eq. (30) exactly due to the finite precision of numerical integrations.

Figure 2 shows the excellent agreement at $r_* = 1$ between the numerical profiles and their analytic near-horizon counterparts in Eqs. (16). Moreover, a striking feature of the radial profiles of $\mathcal{G}r_H^4$ and φ is that they both converge to finite values for all $r_* \geq 1$ when φ_H is increased towards $\varphi_H^{\max}$ despite, meanwhile, the hidden curvature singularity approaching the horizon. Our results provide numerical evidence that as φ_H approaches $\varphi_H^{\max}$, the Gauss-Bonnet scalar reaches the finite value $\mathcal{G}r_H^4 = 48$ as $r_* \to 1$ with $r_* > 1$, as shown in Fig. 3. This value of $\mathcal{G}r_H^4 = 48$ coincides with the first term in the analytic, theory-independent prediction of Eq. (18a). Given these results, it is not clear that a naked singularity arises when one saturates the bound in Eq. (12) (see e.g., [29,35]). We find qualitatively similar behavior for the Gauss-Bonnet scalar and scalar field in the other ESGB theories considered in this paper. We also provide analytical near-horizon expansions of the Ricci and Kretschmann scalars valid for all ESGB theories in Appendix A.

Let us now return to the sensitivity α. As explained below Eq. (27), this quantity must be seen as a function of $\bar{\varphi}$ and of the ratio ℓ/μ. However, we can exploit the theory's shift symmetry to calculate it for all values of ℓ/μ at once. Indeed, the Wald entropy (19) now reads

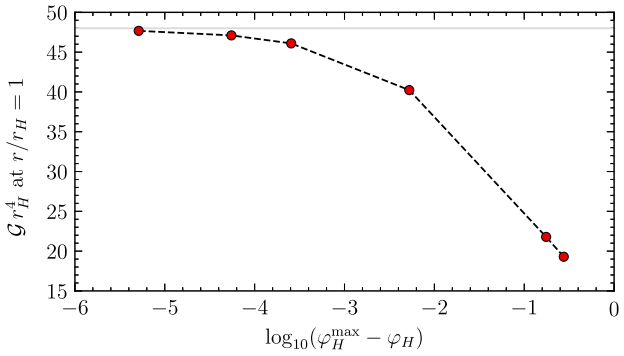

FIG. 3. Numerical Gauss-Bonnet scalar $\mathcal{G}r_H^4$ evaluated at the event horizon $r_* = r/r_H = 1$ for a sequence of black holes with constant $(\ell/\mu)^2 = 10^{-1}$. As the scalar field at the horizon φ_H approaches its maximum allowed value $\varphi_H^{\max} \approx 3.77526$, the Gauss-Bonnet scalar tends to the limit $\mathcal{G}r_H^4 = 48$ (horizontal line) predicted analytically by Eq. (18a).

$$\mathscr{S}_{\rm W} = \pi(r_H^2 + 8\ell^2\varphi_H), \tag{31}$$

and it is linear in φ_H. The sensitivity can therefore only depend on the combination

$$\bar{\varphi} - \frac{\mu^2}{2\ell^2}, \tag{32}$$

which is invariant under a scalar field shift, i.e., under the simultaneous redefinitions $\bar{\varphi} \to \bar{\varphi} + \Delta\varphi$ and $\mu^2 = \mathscr{S}_{\rm W}/4\pi \to$
$\mu^2 + 2\ell^2\Delta\varphi$. This means that the sensitivities of black holes with constant irreducible masses μ_A and μ_B, in shift-symmetric theories with fundamental couplings ℓ_A and ℓ_B respectively, are related to each other as $\alpha_A(\bar{\varphi}) = \alpha_B(\bar{\varphi} + \Delta\bar{\varphi})$ with

$$\Delta\bar{\varphi} = \frac{1}{2}\left(\frac{\mu_B^2}{\ell_B^2} - \frac{\mu_A^2}{\ell_A^2}\right). \tag{33}$$

That this is the case was verified in the perturbative calculation of Ref. [47], but it can also be proven nonperturbatively as follows. Substitute $\varphi = \Phi + \mu^2/(2\ell^2)$ into the differential system (9) with $\ell_*^2 = -1/(8\Phi_H)$ [cf. Eq. (25)], and observe that the result depends on a single parameter, $\Phi_H = \varphi_H - \mu^2/(2\ell^2)$. Then, integrate the system using the initial conditions (13) on the horizon $r_* = 1$, i.e., $N(1) = 0$, $\Phi(1) = \Phi_H$ and $\Phi'(1) = \Phi_H - (\Phi_H^2 - 3/2)^{1/2}$, and note that Φ_H is therefore the only integration constant. The latter can finally be traded for $\bar{\Phi} = \bar{\varphi} - \mu^2/(2\ell^2)$, which is the asymptotic value of Φ at large r_* that coincides with Eq. (32), by inverting $\bar{\Phi}(\Phi_H)$.

In Fig. 4, we therefore show the ADM-to-irreducible mass ratio M/μ (left panel) and sensitivity α (right panel) as functions of the combination of Eq. (32). The top-right panel also includes analytic approximants of α obtained from the Taylor series (28) with $N = 4$, its (2,2)-Padé resummation [47], and the (5,5)-Padé resummation of Eq. (28) pushed to $N = 10$ in this paper. Here $x = 2(\ell/\mu)^2$, and we use Padé approximants to accelerate the convergence of our analytic results. The bottom-right panel shows the relative error between analytic and numerical calculations. We relegate a discussion of the quantity β, deduced from α by means of Eq. (21), to Appendix C.

The agreement between the numerical sensitivity and its (5,5)-Padé counterpart is remarkable, modulo one substantial qualitative difference. The Padé approximants diverge as $\bar{\varphi} - \mu^2/(2\ell^2)$ is increased, and they feature poles as an artifact of the method [88]. By comparison, we find a finite numerical sensitivity, whose curve terminates earlier than that of the (5,5)-Padé approximant, at

$$\bar{\varphi} - \frac{\mu^2}{2\ell^2} \lesssim -1.651. \tag{34}$$

Indeed, the saturation of this inequality coincides numerically with that of the horizon bound (30), which, in turn, is related to the hidden curvature singularity approaching the black hole's horizon, see Fig. 2.

The role of the scalar background $\bar{\varphi}$ of a black hole with fixed Wald entropy $\mathscr{S}_{\rm W} = 4\pi\mu^2$ is therefore the following:

(1) when $\bar{\varphi} \to -\infty$ the black hole decouples from the scalar field, since $\alpha = -Q/M$ (as well as its

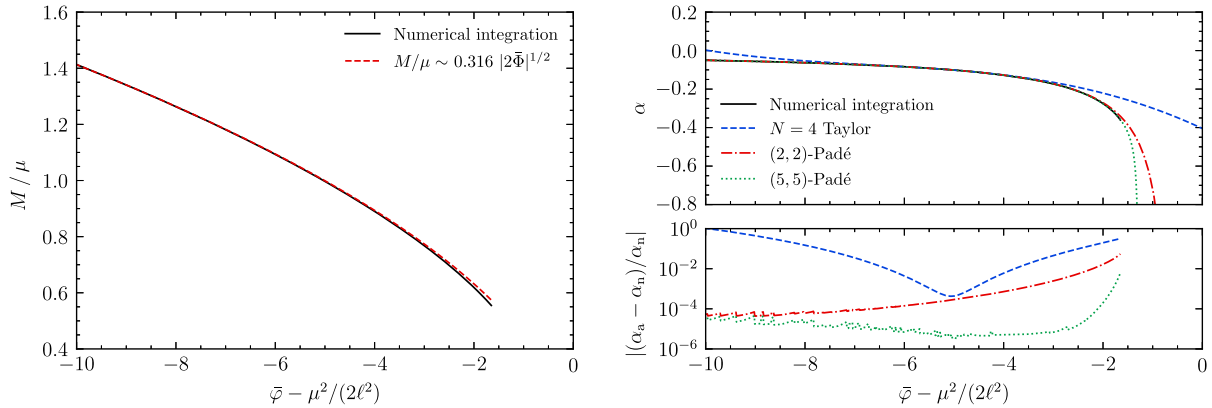

FIG. 4. Black hole mass and sensitivity in the shift-symmetric theory (29) as functions of the quantity $\bar{\varphi} - \mu^2/(2\ell^2)$ introduced in Eq. (32). Left panel: the numerical ADM-to-irreducible mass ratio M/μ. Right panel: the numerical sensitivity α and its analytic estimates from Eq. (28) with $N = 4$, its (2,2)-Padé resummation, and the (5,5)-Padé resummation of Eq. (28) with $N = 10$. The bottom-right panel shows the fractional error between analytic ("a") and numerical ("n") calculations. The numerical sensitivity and its (5,5)-Padé counterpart show excellent agreement, modulo one substantial qualitative difference; the Padé approximant is singular as an artifact of the method, while the numerical sensitivity curve ends at $\bar{\varphi} - \mu^2/(2\ell^2) \approx -1.651$ as we approach saturation of Eq. (30). In the limit $\bar{\Phi} = \bar{\varphi} - \mu^2/(2\ell^2) \to -\infty$, we have $M/\mu = A|2\bar{\Phi}|^{1/2} + \mathcal{O}|\bar{\Phi}|^{-1/2}$ with $A \approx 0.316$ and $\alpha \to 0$, and at the end points we find $M/\mu \approx 0.555$ and $\alpha \approx -0.350$.

derivatives, such as β) vanishes. More precisely, the diagonal (n, n)-Padé approximants with $n \in [1, 5]$ of Eq. (28), which we know up to $N = 10$, all predict $\alpha = 1/(2\bar{\Phi}) + \mathcal{O}(\bar{\Phi}^{-2})$ with $\bar{\Phi} = \bar{\varphi} - \mu^2/(2\ell^2) \to -\infty$. Integrating Eq. (20) then implies

$$M/\mu = A|2\bar{\Phi}|^{1/2} + \mathcal{O}|\bar{\Phi}|^{-1/2}, \tag{35}$$

which fits our numerical results for $A \approx 0.316$. We remark that this fit works remarkably well in the whole range of $\bar{\Phi}$ (see Fig. 4), despite having been obtained only in the range $\bar{\Phi} \in [-10, -9]$;

(2) when $\bar{\varphi}$ is increased, the black hole develops a nonzero and negative sensitivity α, and the hidden curvature singularity approaches the horizon at $\bar{\varphi} - \mu^2/(2\ell^2) \approx -1.651$, where $M/\mu \approx 0.555$, and $\alpha \approx -0.350$ as shown in Fig. 4: see also Eq. (34).

The consequences of point 2 above on adiabatically inspiralling black hole binaries will be investigated in Sec. IV.

B. Dilatonic theory

As a second example, consider the theory

$$f(\varphi) = \frac{1}{4}\exp(2\varphi), \tag{36}$$

such that the action (1) is invariant under the simultaneous redefinitions $\varphi \to \varphi + \Delta\varphi$ and $\ell \to \ell \exp(-\Delta\varphi)$, where $\Delta\varphi$ is a constant. The condition for the existence of a real scalar field at the horizon of constant entropy black holes (26) becomes

$$\varphi_H + \ln\left(\frac{\ell}{\mu}\right) < \frac{1}{2}\ln\left(\frac{4}{1+\sqrt{6}}\right). \tag{37}$$

As with the shift-symmetric case, we can exploit the symmetry of the theory to calculate the sensitivity α for all values of ℓ/μ at once. Indeed, the Wald entropy (19) now reads

$$\mathcal{S}_{\rm W} = \frac{1}{4}[r_H^2 + 4\pi\ell^2 \exp(2\varphi_H)]. \tag{38}$$

As observed in [47], the sensitivities can therefore only depend on the combination

$$\bar{\varphi} + \ln\left(\frac{\ell}{\mu}\right), \tag{39}$$

which is invariant under the simultaneous redefinitions $\bar{\varphi} \to \bar{\varphi} + \Delta\varphi$, $\varphi_H \to \varphi_H + \Delta\varphi$ and $\ell \to \ell \exp(-\Delta\varphi)$, since then $\mu = (\mathcal{S}_{\rm W}/4\pi)^{1/2}$ is also invariant. In other words, the sensitivities of black holes with constant irreducible masses μ_A and μ_B, in dilatonic theories with fundamental couplings ℓ_A and ℓ_B respectively, are related to each other as $\alpha_A(\bar{\varphi}) = \alpha_B(\bar{\varphi} + \Delta\bar{\varphi})$ with

$$\Delta\bar{\varphi} = \ln\left(\frac{\ell_A/\mu_A}{\ell_B/\mu_B}\right). \tag{40}$$

This statement was verified in the perturbative calculation of Ref. [47], but we can again prove it nonperturbatively as follows: substitute $\varphi = \Phi - \ln(\ell/\mu)$ into the differential system (9) with $\ell_* = (\ell/\mu)/(4 - e^{2\Phi_H})^{1/2}$ [cf. Eq. (25)], and observe that the result only depends on one parameter, $\Phi_H = \varphi_H + \ln(\ell/\mu)$. Then, integrate the system using the initial conditions (13) on the horizon $r_* = 1$, i.e., $N(1) = 0$, $\Phi(1) = \Phi_H$ and $\Phi'(1) = -x + (x^2 - 3/2)^{1/2}$ where $x = 2e^{-2\Phi_H} - 1/2$, and note that Φ_H is the only integration constant. The latter can finally be traded for the asymptotic value of Φ, $\bar{\Phi} = \bar{\varphi} + \ln(\ell/\mu)$, which coincides with Eq. (39), by inverting $\bar{\Phi}(\Phi_H)$.

In Fig. 5 we show the ADM-to-irreducible mass ratio M/μ (left panel) and sensitivity α (right panel) as functions of the combination (39). As with Fig. 4, the top-right panel also includes analytic estimates of α derived from the Taylor series (28) with $N = 4$, its (2,2)-Padé resummation [47], and the (5,5)-Padé resummation of Eq. (28) extended to $N = 10$ here, with $x = \ell^2 e^{2\bar{\varphi}}/(2\mu^2)$. We discuss the sensitivity β, obtained from α through Eq. (21), in Appendix C.

As shown by the bottom panel, the agreement between the numerical sensitivity and its (5,5)-Padé counterpart is excellent, except for one substantial qualitative difference. The Padé approximants feature artificial poles, while the numerical sensitivity is finite and its curve terminates earlier than that of the (5,5)-Padé approximant, at

$$\bar{\varphi} + \ln\left(\frac{\ell}{\mu}\right) \lesssim -0.276. \tag{41}$$

We find that the saturation of this inequality indeed coincides numerically with that of the horizon bound (37), which, in turn, indicates that a hidden curvature singularity is approaching the black hole's horizon, in analogy with the shift-symmetric theory.

The role of the scalar background $\bar{\varphi}$ of a fixed Wald entropy black hole therefore resembles the shift-symmetric case:

(1) when $\bar{\varphi} \to -\infty$, the black hole reduces to the Schwarzschild solution, since $M/\mu \to 1$ and $\alpha = -Q/M \to 0$ (as well as its derivatives β), both analytically and numerically;

(2) when $\bar{\varphi}$ is increased, the sensitivity is negative and a hidden curvature singularity approaches the horizon at $\bar{\varphi} + \ln(\ell/\mu) \approx -0.276$, with $M/\mu \approx 0.913$ and $\alpha \approx -0.285$, as shown in Fig. 5; cf. (41).

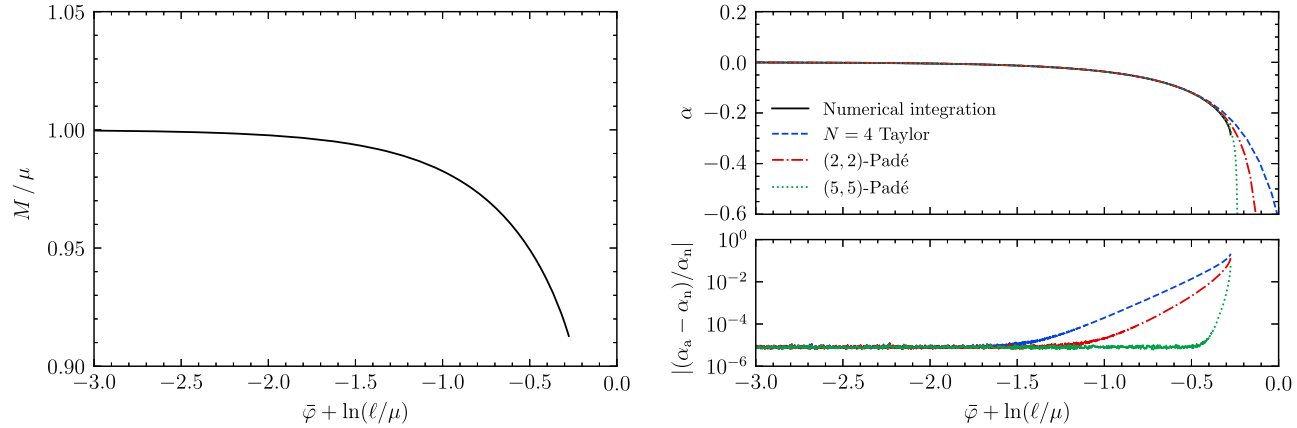

FIG. 5. Black hole mass and sensitivity in the dilatonic theory (36) as functions of the quantity $\bar{\varphi} + \ln(\ell/\mu)$ introduced in Eq. (39). Left panel: the numerical ADM-to-irreducible mass ratio M/μ. Right panel: the numerical sensitivity α and its analytic estimates from Eq. (28) with $N = 4$, its (2,2)-Padé resummation, and the (5,5)-Padé resummation of Eq. (28) with $N = 10$. The bottom-right panel shows the fractional error between analytic ("a") and numerical ("n") calculations. The numerical sensitivity and its (5,5)-Padé counterpart show excellent agreement, expect for one substantial qualitative difference: the Padé approximants are singular as an artifact of the method, while the numerical sensitivity curve ends at $\bar{\varphi} + \ln(\ell/\mu) \approx -0.276$ as we approach saturation of Eq. (37). In the limit $\bar{\varphi} + \ln(\ell/\mu) \to -\infty$ we have $M/\mu \to 1$ and $\alpha \to 0$, and at the end points we find $M/\mu \approx 0.913$ and $\alpha_A \approx -0.285$.

The impact of point 2 above on adiabatically inspiralling black hole binaries will be studied in Sec. IV.

C. Gaussian theory

As a third and last example, consider the theory introduced in Ref. [38],

$$f(\varphi) = -\frac{1}{12}\exp(-6\varphi^2), \tag{42}$$

for which the action (1) is invariant under the $\mathbb{Z}_2$-symmetry transformation $\varphi \to -\varphi$. We note that the Schwarzschild spacetime is a solution of this theory when $\varphi = 0$, since then Eq. (4a) reduces to $R_{\mu\nu} = 0$ and $f_{,\varphi}(\varphi)$ vanishes in Eq. (4b).

For small φ, the coupling can be approximated as

$$f(\varphi) = \frac{1}{2}\varphi^2 + \ldots \tag{43}$$

modulo boundary terms in the action, which is the quadratic model studied in Ref. [39] and developed further in Refs. [89,90]. When the ratio

$$\ell/M \approx 1.704, \quad \text{or} \quad \ell_* = \ell/r_H \approx 0.852 \tag{44}$$

is exceeded, the Schwarzschild spacetime is unstable, and "spontaneously scalarized" black holes with nontrivial scalar field profiles branch off from the Schwarzschild solution [38,39]. In the full Gaussian theory (42), scalarized yet stable black holes were obtained numerically [38], but they are restricted to asymptotically zero scalar fields. In Appendix D we review how these scalarized solutions were found.

Here, we derive the numerical sensitivity of a scalarized black hole as a function of ℓ/μ and of its generically nonzero asymptotic scalar field value $\bar{\varphi}$. Note that a scalarized black hole's sensitivity cannot be estimated from the analytic formula (28), which can only vanish when $\bar{\varphi} = 0$, since then $f'(\bar{\varphi}) = 0$.

The condition for the existence of a real scalar field at the horizon of constant entropy black holes (26) is

$$\frac{\ell^2 e^{-6\varphi_H^2}}{2\mu^2}\left(\sqrt{6}|\varphi_H| - \frac{1}{12}\right) < 1, \tag{45}$$

which is a transcendental equation for φ_H, while the Wald entropy (19) reads

$$\mathcal{S}_{\rm W} = \pi[r_H^2 - (\ell^2/3)\exp(-6\varphi_H^2)]. \tag{46}$$

Using the $\mathbb{Z}_2$ symmetry of the theory, we anticipate from the definition (20) that $\alpha \to -\alpha$ when $\bar{\varphi} \to -\bar{\varphi}$. However, the Gaussian theory lacks further symmetries to obtain α at once for all ℓ/μ ratios, contrary to the shift-symmetric and dilatonic theories. Thus, we focus here on a few illustrative examples, but gather our complete results for values $(\ell/\mu)^2 \leq 20$ with increment $\Delta(\ell/\mu)^2 \approx 0.2$ in [82]. We leave a discussion of the sensitivity β to Appendix C.

In Fig. 6, we show the ADM-to-irreducible mass ratio M/μ (left panel) and sensitivity α (right panel) for five values of the ratio ℓ/μ. For sufficiently small ℓ/μ the curves are single-valued, as shown by the example $(\ell/\mu)^2 = 3.00$. The sensitivity is qualitatively similar to the analytic curves obtained in Ref. [47], Fig. 3, since spontaneous scalarization does not occur at $\bar{\varphi} = 0$ in such cases. Moreover, we always find that $\alpha = 0$ at $\bar{\varphi} = 0$, thus

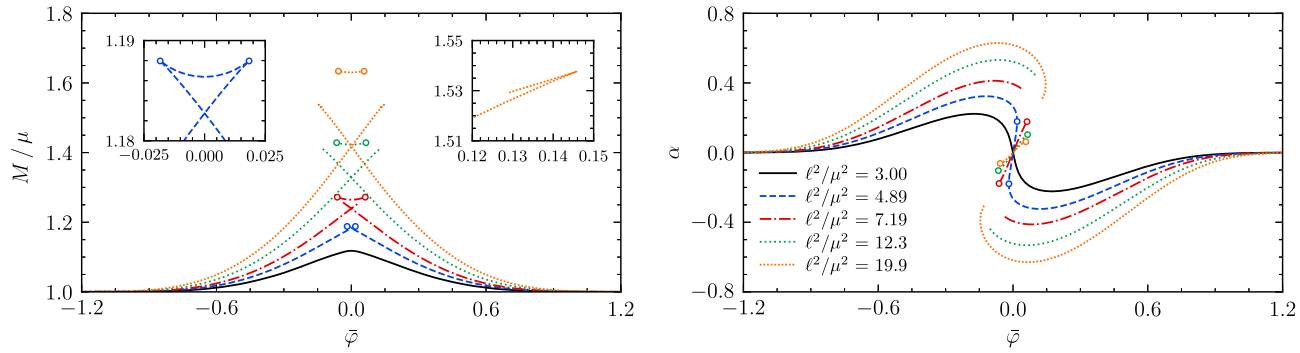

FIG. 6. Black hole mass and sensitivity in the Gaussian theory (42) as functions of $\bar{\varphi}$ and ℓ/μ. We consider five families of constant entropy solutions with $(\ell/\mu)^2 = \{3.00, 4.89, 7.19, 12.3, 19.9\}$, and the legend is shared by both panels. Left panel: the numerical ADM-to-irreducible mass ratio M/μ. Right panel: the numerical sensitivity α. For values $(\ell/\mu)^2 \lesssim 3.82$ the curves include a stable Schwarzschild solution $\alpha = 0$ at $\bar{\varphi} = 0$. For values $(\ell/\mu)^2 \gtrsim 3.82$ the curves are multivalued due to the occurrence of spontaneous scalarization. The segments bracketed by the circles denote the "Schwarzschild branches", which include an unstable Schwarzschild solution $\alpha = 0$ at $\bar{\varphi} = 0$. The remainder of the curves form two "scalarized branches" which include the stable scalarized black holes presented in Appendix D and reviewed in Table I, with $\bar{\varphi} = 0$ but $\alpha \neq 0$. For $(\ell/\mu)^2 \in [3.82, 5.61]$, these three branches are connected. At their junction, M/μ features a cusp, and the slope of α is infinite, cf. $(\ell/\mu)^2 = 4.89$ and the left inset; but when $(\ell/\mu)^2 \gtrsim 5.61$, the branches are discontinuous due to the violation of the horizon bound (45). When $(\ell/\mu)^2 \in [13.6, 13.8]$ and $(\ell/\mu)^2 \gtrsim 14.0$, the ratio M/μ of scalarized branches also features a cusp, cf. $(\ell/\mu)^2 = 19.9$ and the right inset. For all $\bar{\varphi}$ values, M/μ is larger along the Schwarzschild branch than along its scalarized counterparts, and at $\bar{\varphi} = 0$, both scalarized branches have the same M/μ ratio.

recovering a stable Schwarzschild spacetime $\varphi = 0$ at this particular point; see below Eq. (42).

However, when

$$(\ell/\mu)^2 \gtrsim 3.82, \tag{47}$$

the scalarization threshold (44) is exceeded [take $\mu^2 = \mathscr{S}_{\rm W}/4\pi$, where $\mathscr{S}_{\rm W}$ is given by Eq. (46) and $\varphi_H = 0$ for Schwarzschild], and the situation changes. First, the curves become *multivalued*. This is most easily seen for $\bar{\varphi} = 0$, such that α can either be zero, or take two equal and opposite nonzero values, whose magnitude increase with ℓ/μ. The former vanishing α corresponds to an unstable Schwarzschild spacetime, while its latter nonzero values are those of the stable scalarized black holes reviewed in Appendix D, with asymptotically zero scalar fields $\bar{\varphi} = 0$. For clarity, we gather in Table I the correspondence between the values ℓ/μ used here and those of the ratio $\ell_* = \ell/r_H$ used in the literature and in Appendix D, found using Eq. (25).

TABLE I. Scalarized black hole examples in the theory (42), with asymptotically vanishing scalar fields, $\bar{\varphi} = 0$. The values in the first three columns are related to each other by Eq. (25).

$\ell_*^2 = \ell^2/r_H^2$	ℓ^2/μ^2	$\pm\varphi_H$	$\pm\alpha$
1.00	4.89	0.318	0.264
1.56	7.19	0.481	0.394
2.78	12.3	0.614	0.522
4.58	19.9	0.702	0.618

For larger ℓ/μ ratios, the sensitivity curve is increasingly sheared and it can even be discontinuous when $(\ell/\mu)^2 \gtrsim 5.61$, see e.g., $(\ell/\mu)^2 = 7.19$. The discontinuity happens due to the existence of intervals of values of φ_H which do not satisfy the horizon bound (45), but that are encountered while implementing the algorithm given in the beginning of Sec. III. These intervals are shown in the bottom panel of Fig. 12, in Appendix D. As one approaches the saturation of Eq. (45), a hidden curvature singularity resembling that of shift-symmetric theories (cf. Fig. 2) approaches the horizon. Finally, as $\bar{\varphi} \to \pm\infty$, we notice that $M/\mu \to 1$ and $\alpha \to 0$ (as well as β and higher derivatives) for all ℓ/μ values, thus recovering scalar-field-decoupled black holes.

Given a fixed ratio $(\ell/\mu)^2 \gtrsim 3.82$, we will split our curves into the three following segments, or "branches". We name the branch bracketed by the circles in Fig. 6, going through $\alpha = 0$ at $\bar{\varphi} = 0$ and with the largest M/μ ratio at $\bar{\varphi} = 0$, the "Schwarzschild branch". It describes a family of black holes that can be continuously deformed into the Schwarzschild solution through adiabatic changes in $\bar{\varphi}$. We recall that since $(\ell/\mu)^2 \gtrsim 3.82$, the Schwarzschild spacetime (with $\varphi = 0$) is unstable [38,39]. However, the other points with $\bar{\varphi} \neq 0$ belonging to this branch correspond to new black hole spacetimes whose stability is so far unknown. We leave their study to future work. Next, we name the remaining two branches, going through equal and opposite $\alpha \neq 0$ and equal M/μ at $\bar{\varphi} = 0$, the "scalarized branches". They describe two families of black holes that can be continuously deformed into each other through adiabatic changes of $\bar{\varphi}$, and that include, e.g., the stable scalarized black holes listed in Table I at $\bar{\varphi} = 0$. The points

with $\bar{\varphi} \neq 0$ belonging to these branches also represent new black hole solutions, whose stability we also leave to future work.

For $(\ell/\mu)^2 \in [3.82, 5.61]$, the three branches above are connected, see the $(\ell/\mu)^2 = 4.89$ curves in Fig. 6. Hence, in principle, black holes can evolve adiabatically from one branch to another. Note however that M/μ features a cusp at the branches' junction, see the left inset in Fig. 6. The black hole's sensitivity β, defined as the slope of α by Eq. (21), must therefore diverge at the junction, as shown in Appendix C. Finally, for values $(\ell/\mu)^2 \in [13.6, 13.8]$ and $(\ell/\mu)^2 \gtrsim 14.0$, the ratio M/μ of the scalarized branches also features a cusp (while the three branches are always disconnected), as shown by the example $(\ell/\mu)^2 = 19.9$ in the right inset of Fig. 6.

Let us conclude this section with the following observation, which will play an important role below. Consider a scalarized black hole with fixed $(\ell/\mu)^2 \gtrsim 3.82$ and, initially, $\alpha > 0$ ($\alpha < 0$) at $\bar{\varphi} = 0$. Then, $\bar{\varphi}$ cannot be increased (decreased) in adiabatic conditions indefinitely. Indeed, depending on $(\ell/\mu)^2$: either

(1) the black hole flows along the scalarized branch up to a cusp of M/μ, cf. $(\ell/\mu)^2 = 4.89$ or $(\ell/\mu)^2 = 19.9$ in Fig. 6. At the cusp, $\bar{\varphi}$ cannot be increased (decreased) further, or the black hole must leave its branch discontinuously, thus losing adiabaticity, or
(2) the black hole eventually reaches the end point of its scalarized branch, cf. $(\ell/\mu)^2 = 7.19$ and $(\ell/\mu)^2 = 12.3$ in Fig. 6. At the end point, the condition (45) is saturated and a hidden singularity approaches the black hole's horizon.

The consequences of points 1 and 2 above on adiabatically inspiralling black hole binaries will be studied in Sec. IV.

IV. THE FATE OF BLACK HOLE BINARIES

Perhaps the most startling conclusion we drew from Figs. 4 to 6 above is that adiabatic changes to the environmental scalar field $\bar{\varphi}$ of a black hole can induce it to evolve towards a limiting $\bar{\varphi}$ value, beyond which it can no longer be continuously deformed into a black hole with the same Wald entropy.

We can then ask: could this scenario be realized in a black hole binary, where changes to the scalar environment $\bar{\varphi}_A$ of a black hole A are induced by the scalar hair of an inspiralling companion B? The setup is illustrated in Fig. 7.

To answer this question, we use the results of Ref. [47]. There, the PN dynamics of bound binary systems was studied in the weak-field, small orbital velocity limit $\mathcal{O}(M/R) \sim \mathcal{O}(v^2)$. The field equations were solved iteratively around a Minkowski metric $g_{\mu\nu} = \eta_{\mu\nu} + \delta g_{\mu\nu}$, and a constant scalar background φ_0 imposed by the binary's cosmological environment, $\varphi = \varphi_0 + \delta\varphi$. At Newtonian (0PN) order, to which we restrict ourselves here, we thus have [47]

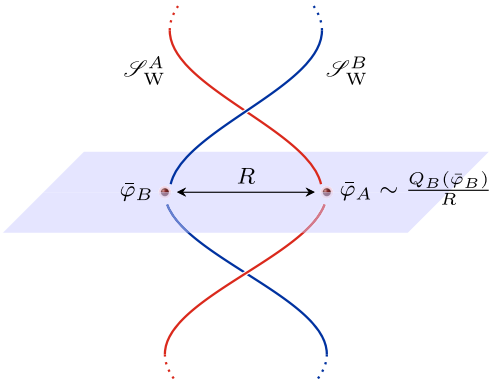

FIG. 7. Illustration of the two-body dynamics. Two black holes with ADM masses and scalar charges $M_A(\bar{\varphi}_A)$, $Q_A(\bar{\varphi}_A) = -M_A(\bar{\varphi}_A)\alpha_A(\bar{\varphi}_A)$ and their B counterparts are inspiralling at fixed irreducible masses μ_A and μ_B. In the previous sections, we calculated these quantities nonperturbatively. The background scalar field $\bar{\varphi}_A$, experienced by black hole A, can now be estimated at leading-order by the $\propto 1/R$ potential (48a) sourced by black hole B, and vice versa. The values of $\bar{\varphi}_A$ and $\bar{\varphi}_B$ change as the orbital radius R decreases.

$$\bar{\varphi}_A = \varphi(t, \boldsymbol{x}_A) = \varphi_0 - \frac{M_B^0 \alpha_B^0}{R} + \mathcal{O}(v^4), \tag{48a}$$

$$\bar{\varphi}_B = \varphi(t, \boldsymbol{x}_B) = \varphi_0 - \frac{M_A^0 \alpha_A^0}{R} + \mathcal{O}(v^4), \tag{48b}$$

where $R = |\boldsymbol{x}_A - \boldsymbol{x}_B|$ is the orbital separation, and where the superscript "0" denotes a quantity evaluated by formally setting $\bar{\varphi}_{A,B} = \varphi_0$. For shift-symmetric and dilatonic models, we can set $\varphi_0 = 0$ without loss of generality, using the symmetries given below Eq. (29) and below Eq. (36). For the Gaussian theory we choose $\varphi_0 = 0$, which corresponds to a nondynamical scalar field on cosmological scales, at least classically [91]. Given a binary system with irreducible masses μ_A and μ_B, and a fundamental coupling value ℓ, the quantities entering Eqs. (48) are then fully evaluated from Figs. 4–6, 5, and 6 by setting formally $\bar{\varphi} = 0$ there, and they hence depend only on the ratios ℓ/μ_A and ℓ/μ_B.

As a minimal value for the orbital radius, we use the light ring $R_{\rm LR}$. Indeed, in general relativity the light ring marks the transition to the ringdown phase in a compact binary evolution, and it can be estimated, e.g., using the effective-one-body (EOB) formalism [92,93]. The EOB framework was generalized to scalar-tensor theories in Refs. [94,95], but the results were shown in Ref. [47] to also include ESGB models. Here we will need the light ring at 0PN,

$$R_{\rm LR} = 3 G_{AB} M, \tag{49}$$

where $M = M_A^0 + M_B^0$, and $G_{AB} = 1 + \alpha_A^0 \alpha_B^0$ is an effective gravitational coupling reflecting the linear addition of the metric and scalar interactions at this order.

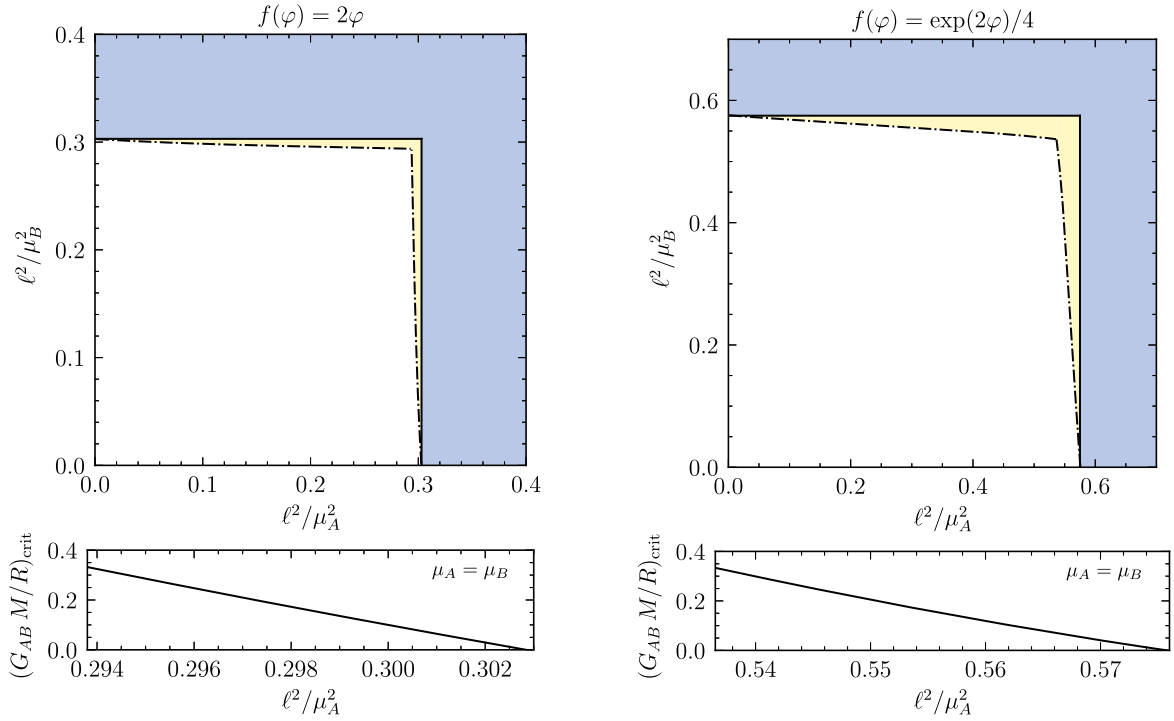

FIG. 8. Parameter space of an inspiralling binary black hole with fixed ratios ℓ/μ_A and ℓ/μ_B in shift-symmetric and dilatonic theories. In the infinite separation limit $R \to \infty$, each black hole is isolated and the conditions (50) and (52) exclude the upper panels' dark (blue) shaded regions. In the light (yellow) shaded regions, the binary is initially regular at infinity, but at least one of the black holes violates the conditions above before the system reaches its light ring (49), i.e., at some critical orbital radius $R_{\rm crit} > R_{\rm LR}$. This signals that this black hole's hidden curvature singularity has reached its horizon. The critical orbital radius $R_{\rm crit}$ is shown by the lower panels for the example of symmetric binary systems $\mu_A = \mu_B$, and it varies between $R_{\rm crit} \to \infty$ and $R_{\rm crit} = R_{\rm LR}$, depending on how close the black holes initially are to saturating (50) or (52). Left panels: in the shift-symmetric case $f(\varphi) = 2\varphi$, isolated black holes must satisfy $(\ell/\mu_A)^2 \lesssim 0.303$. For binaries, this bound is tightened and becomes $(\ell/\mu_A)^2 \lesssim 0.294$ when $\mu_A = \mu_B$. Right panels: in the dilatonic case $f(\varphi) = \exp(2\varphi)/4$, isolated black holes must satisfy $(\ell/\mu_A)^2 \lesssim 0.576$. For binaries, this bound is tightened and becomes $(\ell/\mu_A)^2 \lesssim 0.536$ when $\mu_A = \mu_B$.

In the following, we explore whether adiabatically readjusting black holes can be driven outside their domain of existence in an inspiralling binary black hole system with orbital radius $R > R_{\rm LR}$ for shift-symmetric, dilatonic, and Gaussian models.

A. Shift-symmetric theory

When $f(\varphi) = 2\varphi$, we have from Fig. 4 that both black holes in a binary must satisfy the condition (34),

$$\bar{\varphi}_A - \frac{\mu_A^2}{2\ell^2} \lesssim -1.651, \tag{50a}$$

$$\bar{\varphi}_B - \frac{\mu_B^2}{2\ell^2} \lesssim -1.651. \tag{50b}$$

In the early inspiral regime, $R \to \infty$ and both $\bar{\varphi}_A$ and $\bar{\varphi}_B$ vanish, see Eqs. (48) and below. The conditions above then yield $(\ell/\mu_A)^2 \lesssim 0.303$ and $(\ell/\mu_B)^2 \lesssim 0.303$, which excludes the dark (blue) shaded region in the upper-left panel of Fig. 8. In this regime, the Gauss-Bonnet coupling ℓ is bounded from above; it must be smaller than a fraction of each black holes' fixed Wald entropies $\mathcal{S}_{\rm W}^A = 4\pi\mu_A^2$ and $\mathcal{S}_{\rm W}^B = 4\pi\mu_B^2$. Our result is consistent with previous constraints obtained in, e.g., Ref. [51] for isolated black holes with constant ADM masses.

However, in general $\bar{\varphi}_A$ and $\bar{\varphi}_B$ are nonzero and positive [cf. Eq. (48)], α_A^0 and α_B^0 being negative and given in Fig. 4, and they increase as the orbital radius R decreases. This effectively tightens the conditions (50) gradually along the inspiral, and extends the excluded parameter space, as depicted by the light (yellow) shaded region. For any point in the latter, there indeed exists a critical orbital radius $R_{\rm crit} > R_{\rm LR}$ where at least one of the conditions (50) is saturated. As discussed in Sec. III A, this signals that at least one of the black holes' hidden singularity is approaching its horizon, see point 2 there. At the border with the white region, we have $R_{\rm crit} = R_{\rm LR}$.

The light (yellow) shaded region is here relatively narrow, because the influence of black hole A on $\bar{\varphi}_B$ is limited by the assumption $R > R_{\rm LR}$, and the fact that $\alpha_A^0 \approx -0.350$ at most, see Fig. 4. The region also shrinks when, say, $(\ell/\mu_A)^2 \ll 1$, because then black hole A decouples from the scalar field, and it cannot affect $\bar{\varphi}_B$ since $\alpha_A^0 \to 0$.

Conversely, the region is thickest for symmetric binaries $\mu_A = \mu_B$, yielding a tighter bound $(\ell/\mu_A)^2 \lesssim 0.294$. Finally, conditions (50) are always satisfied down to $R_{\rm LR}$ in the white region.

The lower-left panel of Fig. 8 shows the 0PN potential value $G_{AB}M/R_{\rm crit}$ at criticality, that is when Eqs. (50) saturate, for the example of symmetric binaries, $\mu_A = \mu_B$. This potential is related to the binary's orbital velocity $\dot{\phi} = {\rm d}\phi/{\rm d}t$ via Kepler's law (see e.g., Ref. [73]),

$$\frac{G_{AB}M}{R_{\rm crit}} = (G_{AB}M\dot{\phi}_{\rm crit})^{2/3} + \mathcal{O}(v^4), \tag{51}$$

and its numerical value varies from $1/3$ ($R_{\rm crit} = R_{\rm LR}$) to zero ($R_{\rm crit} \to \infty$) as we move along the line $\mu_A = \mu_B$, across the light (yellow) shaded region of the upper panel.

B. Dilatonic theory

The steps presented above are now easily adapted to the dilatonic case. When $f(\varphi) = (1/4)\exp(2\varphi)$, we have from Fig. 5 that a binary black hole must satisfy two copies of the condition (41),

$$\bar{\varphi}_A + \ln\left(\frac{\ell}{\mu_A}\right) \lesssim -0.276, \tag{52a}$$

$$\bar{\varphi}_B + \ln\left(\frac{\ell}{\mu_B}\right) \lesssim -0.276. \tag{52b}$$

In the limit $R \to \infty$, both $\bar{\varphi}_A$ and $\bar{\varphi}_B$ vanish (48), and the conditions above yield $(\ell/\mu_A)^2 \lesssim 0.576$ and $(\ell/\mu_B)^2 \lesssim 0.576$. The resulting excluded dark (blue) shaded region is shown in the upper-right panel of Fig. 8. When the orbital radius R is finite, $\bar{\varphi}_A$ and $\bar{\varphi}_B$ are nonzero and the conditions (52) extend the excluded parameter space, as shown by the light (yellow) shaded region. Just as with the shift-symmetric case, for each point in this region there exists a critical orbital radius $R_{\rm crit} > R_{\rm LR}$ at which at least one of the conditions (52) is saturated. As discussed in Sec. III B, the latter signals that one of the black holes' hidden singularities is approaching its horizon, see point 2 there. The region is thickest when $\mu_A = \mu_B$, in which case the Gauss-Bonnet coupling is bounded by $(\ell/\mu_A)^2 \lesssim 0.536$.

The critical Newtonian potential $G_{AB}M/R_{\rm crit}$ is shown in the lower panel for $\mu_A = \mu_B$, and it varies from $1/3$ when $R_{\rm crit} = R_{\rm LR}$, to zero when $R_{\rm crit} \to \infty$.

C. Gaussian theory

The Gaussian case is perhaps the most striking, but it must also be treated most carefully. As discussed in Subsection III C, when $(\ell/\mu_A)^2 \gtrsim 3.82$ a black hole A can in principle either belong to a Schwarzschild branch or to one of its two scalarized counterparts. However, in this paper we choose the quantity φ_0, which the environment $\bar{\varphi}_A$ of the black hole reduces to when $R \to \infty$, to be zero [cf. Eq. (48) and below]. Given such initial conditions, the black hole must belong to a scalarized branch, since otherwise it would reduce initially to an unstable Schwarzschild black hole. When $(\ell/\mu_A)^2 \gtrsim 3.82$, we therefore start from scalarized black holes such as those presented in Table I and typically discussed in the literature, and when $(\ell/\mu_A)^2 \lesssim 3.82$, from stable Schwarzschild black holes.

Figure 9 shows the parameter space of an inspiralling black hole binary with fixed ratios ℓ^2/μ_A^2 and ℓ^2/μ_B^2, which we explored for $(\ell/\mu_{A,B})^2 \leq 20$ with increments in $\Delta(\ell/\mu_{A,B})^2 \approx 0.2$. In region ①, at least one of the black holes, say A, satisfies $(\ell/\mu_A)^2 \lesssim 3.82$. As shown by Fig. 6 on the example $(\ell/\mu_A)^2 = 3.00$, we have $\alpha_A^0 = 0$ and thus $\bar{\varphi}_B = 0$ by Eq. (48). Since, moreover, black hole A exists for all $\bar{\varphi}_A$ values, any point in region ① represents a binary system that can adiabatically inspiral until merger.

Next, we take $(\ell/\mu_A)^2 \gtrsim 3.82$ and $(\ell/\mu_B)^2 \gtrsim 3.82$, corresponding to two initially scalarized black holes such as those of Table I, which evolve along their respective scalarized branches as they inspiral, see Fig. 6. We note that for every $\ell/\mu_{A,B}$ values we considered, the sensitivities at infinity $\alpha_{A,B}^0$ are always defined, contrary to shift-symmetric and dilatonic theories, which exclude the dark (blue) shaded regions of Fig. 8.

Let us consider two scalarized black holes with sensitivities α_A and α_B of the same sign, taken to be positive without loss of generality. Then, $\alpha_{A,B}^0 > 0$, so $\bar{\varphi}_{A,B}$ are both negative [cf. Eq. (48)], with increasing magnitudes as the orbital radius R decreases. The black holes gradually drive each other away from the cusps or end points of their respective branches, see Fig. 6. Hence, scalarized black hole binaries with sensitivities of the same sign can adiabatically inspiral until merger.

The picture above changes radically if the scalarized black holes $(\ell/\mu_A)^2 \gtrsim 3.82$ and $(\ell/\mu_B)^2 \gtrsim 3.82$ have sensitivities α_A and α_B with opposite signs. Indeed, if $\alpha_A^0 > 0$ and $\alpha_B^0 < 0$, then $\bar{\varphi}_A \geq 0$ and $\bar{\varphi}_B \leq 0$, with increasing absolute values as R decreases. We recover the situation described by points 1 and 2 at the end of Sec. III C. As shown by the shaded regions of Fig. 9, the parameter space is then almost entirely excluded. More precisely, for any point of region ②, there exists a critical orbital radius $R_{\rm crit} > R_{\rm LR}$ where at least one of the black holes, described by point 1, cannot inspiral further without leaving its branch discontinuously at $R_{\rm crit}$. For any point of region ③, at least one black hole is described by point 2 and at some $R_{\rm crit} > R_{\rm LR}$, its hidden curvature singularity approaches the horizon. In the limit $\ell/\mu_A \gg \ell/\mu_B$, α_A^0 is large and we find that black hole B always completes the scenario 1 or 2 before A. The shaded regions are delimited by ℓ/μ_B intervals that reduce to those observed above points 1 and 2 of Sec. III C; when $(\ell/\mu_B)^2 \in [3.82, 5.61], [13.6, 13.8]$ and $(\ell/\mu_B)^2 \gtrsim 14.0$, the black hole B is described

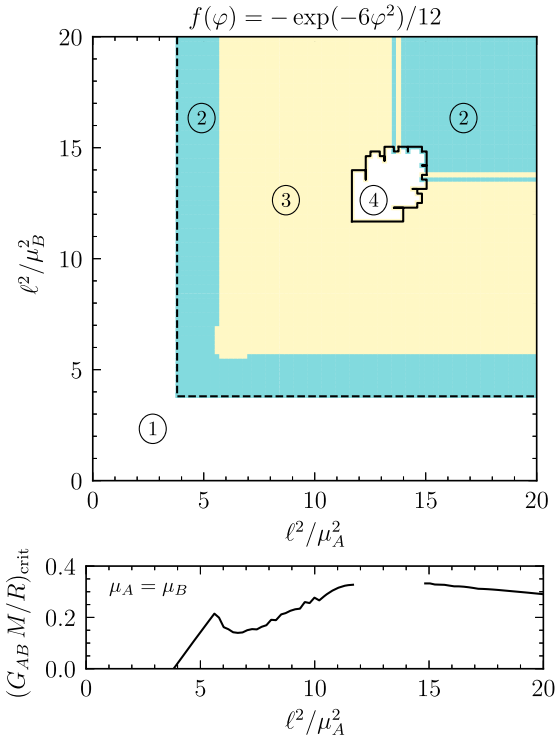

FIG. 9. Parameter space of an inspiralling binary black hole with fixed ℓ/μ_A and ℓ/μ_B and initially vanishing scalar field environments $\varphi_0 = 0$ in the Gaussian theory. The black hole A reduces initially to the Schwarzschild solution when $(\ell/\mu_A)^2 \lesssim 3.82$, and to a scalarized black hole when $(\ell/\mu_A)^2 \gtrsim 3.82$. In region ①, at least one black hole is initially Schwarzschild and the system can inspiral adiabatically until merger. When $(\ell/\mu_A)^2 \gtrsim 3.82$ and $(\ell/\mu_B)^2 \gtrsim 3.82$, each inspiralling black hole evolves along a scalarized branch such as those presented in Fig. 6. When their sensitivities α_A and α_B have the same sign, they can inspiral adiabatically until merger, but when α_A and α_B have opposite signs, almost the entire parameter space is excluded, as shown by the shaded regions. In region ②, at least one of the black holes meets point 1 of Sec. III C at some $R_{\rm crit} > R_{\rm LR}$ and must leave its scalarized branch discontinuously there. In region ③, a black hole meets point 2 at $R_{\rm crit} > R_{\rm LR}$, meaning that its hidden curvature singularity reaches its horizon there. The remaining parameter space that allows the system to inspiral adiabatically until merger is comparatively small, and depicted by region ④. In the limit $\ell/\mu_A \gg \ell/\mu_B$, we have $|\alpha_A^0| \gg |\alpha_B^0|$ so that black hole B always completes the scenario 1 or 2 before A. Then region ② is delimited by the ranges $(\ell/\mu_B)^2 \in [3.82, 5.61]$, $[13.6, 13.8]$ and $(\ell/\mu_B)^2 \gtrsim 14.00$ discussed in Sec. III C. The critical orbital radius $R_{\rm crit} > R_{\rm LR}$ at which points 1 or 2 indifferently happen is shown by the lower panel for $\mu_A = \mu_B$ (but $\alpha_A = -\alpha_B$). It varies between $R_{\rm crit} \to \infty$ and $R_{\rm crit} = R_{\rm LR}$.

by point 1, and in the complementary intervals it is described by point 2. The remaining allowed region ④ is comparatively small. There, the black holes live on a sufficiently large scalar environment range, while keeping their scalar charges small enough for neither scenario 1 nor 2 to happen.

The critical Newtonian potential $G_{AB}M/R_{\rm crit}$ at which indifferently 1 or 2 happen is shown in the lower panel of Fig. 9 for $\mu_A = \mu_B$, and hence $\alpha_A = -\alpha_B$. It varies between $1/3$ when $R_{\rm crit} = R_{\rm LR}$ and zero when $R_{\rm crit} \to \infty$.

D. Epilogue

In this section, we considered shift-symmetric, dilatonic and Gaussian ESGB models. In all three cases, we found parameter spaces such that the adiabatic inspiral of black hole binaries must break down. Let us conclude with the following remarks.

First, we estimated the scalar environments $\bar{\varphi}_{A,B}$ of each black hole using a Newtonian, leading-order approximation for simplicity. Therefore, our results should not be considered as definitive, but they suggest an interesting parameter space to be further explored, e.g., at higher PN order [47], or using numerical relativity [51,55–58] to reveal the ultimate fate of the black holes. Note however that the phenomena we found can happen in the weak field regime. As shown by the bottom panel of Fig. 8 in shift-symmetric and dilatonic theories, a black hole A can be adiabatically driven to the end point of its sensitivity curve arbitrarily far into the Newtonian regime $G_{AB}M/R \ll 1$, provided that ℓ/μ_A is large enough. In Gaussian theories, a black hole with ratio ℓ/μ_A just above the scalarization threshold $(\ell/\mu_A)^2 \approx 3.82$ must discontinuously leave its scalarized branch very early in the inspiral $G_{AB}M/R \ll 1$, see the bottom panel of Fig. 9. As for the sensitivities α, we recall that they were obtained nonperturbatively.

Second, the adiabatic analysis we performed describes binary systems in the limit where tidal and out-of-equilibrium effects can be discarded. The fact that the adiabatic analysis formally breaks down might signal the occurrence of nonperturbative out-of-equilibrium phenomena. It will hence be important to study the stability of the new black holes with nonzero asymptotic scalar fields presented here. In particular, addressing dynamical (de)scalarization phenomena [57] in ESGB gravity might complete the scenario 1 found in Sec. III C.

Third, in all ESGB models considered, we found parameter space regions such that the hidden singularities of black holes can approach their horizons before merger, cf. point 2 in Sec. III C in the Gaussian case. Unless the black holes then "reopen" into other compact objects [96], the theories might simply not predict any binary evolution once 2 has happened.

If the predictions of this section are qualitatively confirmed in the future, while none of the scenarios listed above are observed in currently available and future gravitational wave event candidates, then new interesting constraints on ESGB theories might be obtained. In particular, scalarized binary black holes with opposite scalar charges might be severely constrained.

V. CONCLUSIONS

We introduced a method to numerically calculate the sensitivities of nonrotating black holes in ESGB theory. This complements the analytical, but perturbative, calculation of Ref. [47], which we also generalized here by calculating higher-order terms in the perturbative series. In the subclasses of this theory where comparison was possible, we showed that analytical and numerical approaches agree remarkably well. The numerical approach also allowed us to calculate the sensitivities of spontaneously scalarized black holes for the first time. We arrived, through a restrictive PN analysis, at the surprising conclusion that adiabatically inspiralling black holes in some of these theories can in principle be driven outside their domain of existence. It would be interesting to confirm this finding by working to higher PN orders or through numerical relativity simulations [51,55–58].

Our results are important for the PN description of black hole binaries in ESGB gravity [43,47–49,97,98], including gravitational waveform predictions [49,50], allowing to finally specialize them to scalarized black hole binaries. Our work could also be used to develop an effective action model [99] of dynamical *black hole* descalarization [57] and explore further the differences with respect to *neutron star* binaries in scalar-tensor theories [100–105] that predict spontaneous scalarization [106].

More broadly, the method introduced here can, in principle, also be used to calculate the sensitivities of black holes in other gravity theories, e.g., the effective field theory introduced in [21], the effective field theory for black hole scalarization of [90], the models of [107–109], and generalizations of ESGB gravity with multiple scalar fields [110]. Indeed, we expect the sensitivities, as calculated here, to play a role beyond ESGB theories: see Refs. [71,83] for another example. Hence, it is desirable that future work on black holes in modified gravity theories study how the black hole "charges" vary as a function of the theory parameters, but also of the asymptotic value of the scalar field (if any) at fixed Wald entropy.

Our findings open some avenues for future work. First, we could analyze the stability of the constant-entropy sequence of solutions for the Gaussian theory studied in Sec. III C. It is known that the equations describing gravitational perturbations of such black holes can cease to be hyperbolic [111–113], suggesting that their time evolution becomes ill-posed. Taking this fact in consideration could in principle shrink further the exclusion regions in Fig. 9, but more work is needed to draw definite conclusions.

Finally, in preparation to model the binary dynamics of spinning black holes in ESGB gravity, one could extend the calculation done here to rotating black holes. The inclusion of spin would introduce a "moment of inertia sensitivity" analogous to that of neutron stars in scalar-tensor theories [70]. In the Gaussian model, it would be particularly interesting to compute the sensitivities of the spin-induced scalarized black holes of Refs. [41,42].

ACKNOWLEDGMENTS

We thank Carlos A. R. Herdeiro, Mohammed Khalil, Eugen Radu, Jan Steinhoff, and Helvi Witek for numerous discussions. We also thank Alessandra Buonanno and Harald Pfeiffer for questions that helped us improve parts of the text. H. O. S. and N. Y. are supported by NASA Grants No. NNX16AB98G and No. 80NSSC17M0041. N. Y. also acknowledges support from the Simons Foundation through Award No. 896696. F.-L. J. and E. B. are supported by NSF Grants No. PHY-1912550, No. AST-2006538, No. PHY-090003, and No. PHY-20043, and NASA Grants No. 17-ATP17-0225, No. 19-ATP19-0051, and No. 20-LPS20-0011. The figures in this work were produced with Matplotlib [114] and TikZ [115]. This work has received funding from the European Union's Horizon 2020 research and innovation programme under the Marie Skłodowska-Curie Grant Agreement No. 690904 and networking support by the GWverse COST Action CA16104, "Black holes, gravitational waves and fundamental physics".

APPENDIX A: NEAR-HORIZON EXPANSION OF THE RICCI AND KRETSCHMANN CURVATURE INVARIANTS

In Sec. II B, we obtained the coefficients of the power series expansions (10) up to φ_4^H, N_4^H, and σ_3^H. We then computed the scalar field and Gauss-Bonnet invariant as in Eqs. (16). We can use the same coefficients to calculate the Ricci and Kretschmann curvature invariants R and $\mathcal{K} = R^{\mu\nu\rho\sigma}R_{\mu\nu\rho\sigma}$ as

$$Rr_H^2 = \rho_H + \sum_{n=1}^{2} \rho_n^H (r_* - 1)^n + \mathcal{O}(r_* - 1)^3, \tag{A1a}$$

$$\mathcal{K} r_H^4 = k_H + \sum_{n=1}^{2} k_n^H (r_* - 1)^n + \mathcal{O}(r_* - 1)^3, \tag{A1b}$$

where the coefficients are long functions of ℓ_* and φ_H available online [82]. Near the saturation of the horizon bound (12), i.e., for $\epsilon^2 = 1 - 24\ell_*^4 f_{,\varphi}(\varphi_H)^2 \ll 1$, we find

$$\rho_H = 2 + \mathcal{O}(\epsilon), \tag{A2a}$$

$$\rho_1^H = -18\frac{\chi}{\epsilon} + \mathcal{O}(\epsilon^0), \tag{A2b}$$

$$\rho_2^H = \frac{243}{16}\frac{\chi^2}{\epsilon^3} + \mathcal{O}(\epsilon^{-2}), \tag{A2c}$$

and

$$k_H = 84 + \mathcal{O}(\epsilon), \tag{A3a}$$

$$k_1^H = -648\frac{\chi}{\epsilon} + \mathcal{O}(\epsilon^0), \tag{A3b}$$

$$k_2^H = \frac{2187}{4}\frac{\chi^2}{\epsilon^3} + \mathcal{O}(\epsilon^{-2}), \tag{A3c}$$

with $\chi = 3 + 4\ell_*^2 f_{,\varphi\varphi}(\varphi_H)$. As with the Gauss-Bonnet scalar, we have that ρ_H and k_H are finite and do not depend on $f(\varphi)$ in this limit, while the other coefficients in Eqs. (A2)–(A3) are singular. The near-horizon expansion of the curvature invariant $R^{\mu\nu}R_{\mu\nu} = (\mathcal{K} + R^2 - \mathcal{G})/4$ can then be inferred from our results, and its first term is finite too.

APPENDIX B: NUMERICAL METHODS

For all our numerical calculations, we used *Mathematica*'s differential equation solving function NDSolve, with the method "StiffnessSwitching", that automatically changes between a nonstiff or stiff solver when necessary. We set both PrecisionGoal and AccuracyGoal to 15, and worked with the default WorkingPrecision. The integrations of Eqs. (9) were performed in the domain $r_* \in [1 - 10^{-\epsilon}, 10^{10}]$, with $\epsilon = 5$. An exception is in the near-horizon integrations done in Sec. III A cf. Fig. 2. There we set WorkingPrecision to machine precision and $\epsilon = 6$.

To calculate the asymptotic parameters M_*, Q_*, and $\bar{\varphi}$ in Eqs. (14), we proceeded as follows. First, from the numerical integration we know the values of φ, φ', and N at our "numerical infinity", $r_* = 10^{10}$. Then, the value φ at $r = r_* = 10^{10}$ gives $\bar{\varphi}$, since for $r_* \gg 1$ all $1/r_*$ corrections are negligible. Next, the values of N and φ' are respectively used in the right-hand sides of Eq. (14a) and of Eq. (14c) (after taking a derivative with respect to r_*). This constitutes a system of two equations for the two unknowns M_* and Q_*, which is then solved with *Mathematica*'s NSolve function. As a consistency check, we verified that M_* calculated this way agrees with the directly evaluation of Eq. (6) at $r_* = 10^{10}$.

APPENDIX C: BLACK HOLE SENSITIVITY β

We gather here the sensitivities β of black holes in the shift-symmetric, dilatonic, and Gaussian theories, obtained from the numerical and analytic sensitivities α of Figs. 4, 5, and 6using Eq. (21) (recall that a fixed $\mathscr{S}_{\rm W}$ is equivalent to a fixed μ). They are useful in the context of PN calculations. For instance, they enter the 1PN Lagrangian of Ref. [47].

In Fig. 10 we show β in the shift-symmetric (left panel) and dilatonic (right panel) cases. We see once more the remarkable agreement between the numerical sensitivities and their (5,5)-Padé counterparts. For a black hole with fixed irreducible mass μ in the shift symmetric case, we find $\beta \to 0$ for $\bar{\varphi} \to -\infty$ and $\beta = -0.376$ at the end point. In the dilatonic case, we have $\beta \to 0$ for $\bar{\varphi} \to -\infty$ and $\beta \approx -1446$ at the end point.

In Fig. 11, we show β in the Gaussian case, for the ℓ/μ values chosen in Fig. 6. When $(\ell/\mu)^2 \lesssim 3.82$, the spontaneous scalarization of Schwarzschild black holes ($\varphi = 0$) does not occur, and we found $\alpha = 0$ at $\bar{\varphi} = 0$ in Fig. 6. By contrast, the sensitivity β of these stable Schwarzschild black holes is nonzero at $\bar{\varphi} = 0$, and it can even be large and finite, cf. $(\ell/\mu)^2 = 3.00$ in Fig. 11. Above the scalarization threshold, a Schwarzschild branch with $\beta > 0$ bracketed by the circles appears, together with two scalarized branches. Given

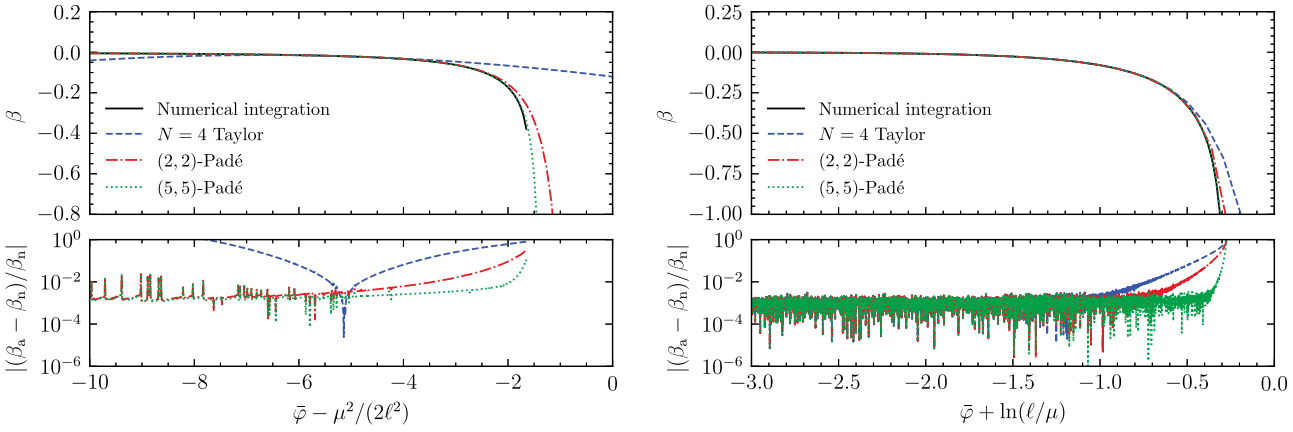

FIG. 10. Black hole sensitivities β obtained from α in Figs. 4 and 5 using the definition (21). Left panel: the sensitivity β in the shift-symmetric case as a function of $\bar{\varphi} - \mu^2/(2\ell^2)$, cf. Eq. (32). Right panel: the sensitivity β in the dilatonic case as a function of $\bar{\varphi} + \ln(\ell/\mu)$ cf. Eq. (39). The upper panels show numerical and analytic results obtained from Eq. (28) with $N = 4$, its (2,2)-Padé resummation, and the (5,5)-Padé resummation of Eq. (28) with $N = 10$. The bottom panels show the fractional error between analytic ("a") and numerical ("n") calculations. The numerical sensitivities and their (5,5)-Padé counterpart show excellent agreement, except for one qualitative difference: the Padé approximants are singular, while the numerical curves end at $\bar{\varphi} - \mu^2/(2\ell^2) \approx -1.651$ and $\bar{\varphi} + \ln(\ell/\mu) \approx -0.276$ as one approaches the saturation of the theories' respective horizon bounds (30) and (37). In the limit $\bar{\varphi} \to -\infty$ we have $\beta \to 0$ for both theories, and at the end points we find $\beta = -0.376$ and $\beta = -1446$, respectively.

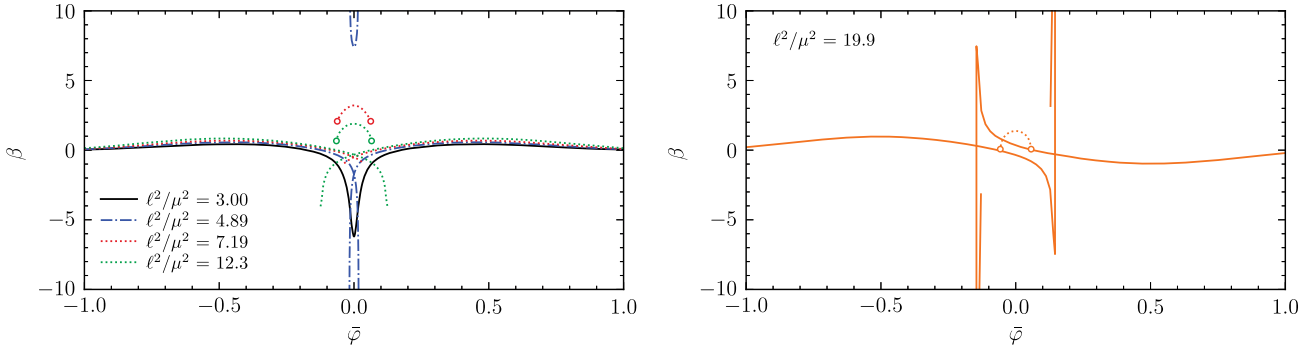

FIG. 11. Black hole sensitivities β in the Gaussian theory as functions of $\bar{\varphi}$ and ℓ/μ. We consider the same constant entropy solutions as in Fig. 6. For values $(\ell/\mu)^2 \lesssim 3.82$ the curve includes a stable Schwarzschild solution at $\bar{\varphi} = 0$, with $\alpha = 0$, but $\beta < 0$ can be large, cf. $(\ell/\mu)^2 = 3.00$. When $(\ell/\mu)^2 \gtrsim 3.82$ the curve is multivalued. The segments bracketed by the circles denote the "Schwarzschild branches" with $\beta > 0$. They include an unstable Schwarzschild solution at $\bar{\varphi} = 0$, with $\alpha = 0$. The remainder of the curves form two "scalarized branches" that include the stable scalarized black holes with $\bar{\varphi} = 0$ and $\alpha \neq 0$. For $(\ell/\mu)^2 \in [3.82, 5.61]$, the three branches are connected. At their junction, M/μ features a cusp, cf. Fig. 6, and the slope of α, that is β here, is infinite. When $(\ell/\mu)^2 \gtrsim 5.61$, the branches are discontinuous due to the violation of the horizon bound (45). But when $(\ell/\mu)^2 \in [13.6, 13.8]$ and $(\ell/\mu)^2 \gtrsim 14.0$, the ratio M/μ of scalarized branches also features a cusp and β hence diverges. This is illustrated with $(\ell/\mu)^2 = 19.9$ in the right panel.

the definition (21), the sensitivities β of the latter are even-symmetrical due to the theory's $\mathbb{Z}_2$ symmetry. We recall that when $3.82 \lesssim (\ell/\mu)^2 \lesssim 5.61$, the branches are connected. As shown, e.g., for the example $(\ell/\mu)^2 = 4.89$ in Fig. 6, M/μ features a cusp at their junction. This means that the slope of α, i.e., β in Fig. 11, is infinite there. When $(\ell/\mu)^2 \gtrsim 5.61$, the branches are discontinuous, cf. $(\ell/\mu)^2 = 7.19$ and $(\ell/\mu)^2 = 12.30$ in Fig. 11. The discontinuity happens due to the existence of φ_H ranges that do not satisfy the horizon bound (45). Our results for values $(\ell/\mu)^2 \leq 20$ in $\Delta(\ell/\mu)^2 \approx 0.2$ increment can be found in [82].

APPENDIX D: OBTAINING SPONTANEOUSLY SCALARIZED BLACK HOLES

We briefly review here how spontaneously scalarized black hole solutions have been obtained in the literature [38,39] for the example of the Gaussian theory (42), when the scalar field vanishes asymptotically.

We first choose a pair of values $\ell_* = \ell/r_H$ and φ_H, and numerically integrate Eqs. (9) outwards, from $r_* = r/r_H = 1$ up to a large value of r_*, and we extract the asymptotic scalar field value $\bar{\varphi}$. We repeat these steps for a range of φ_H values allowed by the reality condition (12), while keeping ℓ_* fixed. The outcome is a function $\bar{\varphi}(\varphi_H)$ that generally has a single zero at $\varphi_H = 0$ corresponding to the Schwarzschild solution [cf. below Eq. (42)]. However, for certain disjoint ℓ_* ranges, an additional even number of zeros with equal and opposite $\varphi_H \neq 0$ appear. They correspond to scalarized black holes, which come in pairs due to the theory's $\mathbb{Z}_2$-symmetry.

The pair of solutions with smallest $|\varphi_H|_0$ values has a nodeless scalar field configuration ("ground state"), while solutions with successively increasing $|\varphi_H|_k$ values

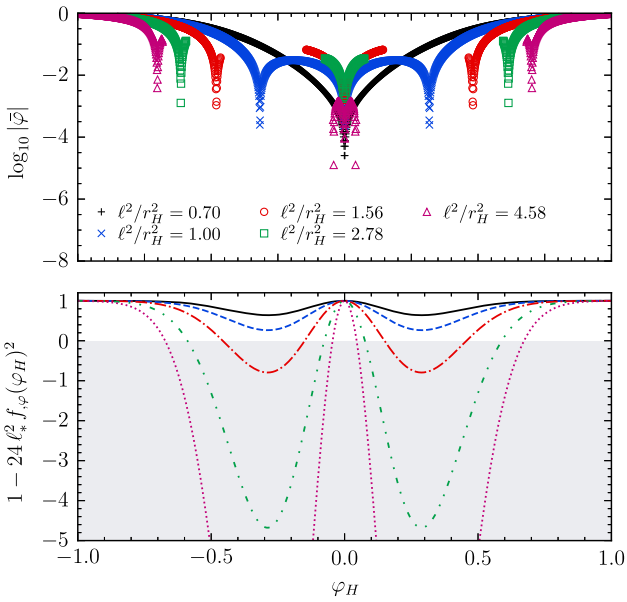

FIG. 12. Finding scalarized black hole solutions in the Gaussian theory (42). Top panel: the asymptotic value $\log_{10}|\bar{\varphi}|$ of the scalar field as a function of its value at the horizon φ_H for several ratios $\ell_* = \ell/r_H$. When $\ell_*^2 \lesssim 0.725$ only one zero of $\bar{\varphi}$, located at $\varphi_H = 0$ exists as shown by the cusps in the data points. It corresponds to the Schwarzschild solution. As we increase ℓ_*, two additional zeros of $\bar{\varphi}$ with $\varphi_H \neq 0$ appear. They have the same magnitude, but opposite signs, as expected from the theory's $\mathbb{Z}_2$-symmetry. Note that for $\ell_*^2 = 1.56$, 2.78 and 4.58 the curve is not continuous. Bottom panel: the existence condition (12) as a function of φ_H. The solid, dashed, dot-dashed, dash-double-dotted, and dotted lines correspond respectively to $\ell_*^2 = \{0.7, 1.0, 1.56, 2.78, 4.58\}$. In the shaded region, Eq. (12) is violated. For $\ell_*^2 = 1.56$, 2.78, and 4.58, the condition is violated on φ_H intervals. This causes the discontinuity in the data points with the same values of ℓ_* in the top panel.

correspond to scalar field configurations with k nodes ("excited states"). In the first ℓ_* range (with smallest ℓ_* values) allowing for spontaneous scalarization, only ground states with $k = 0$ are found. In the second ℓ_* range, $k = 0$ states and their excited $k = 1$ counterparts are observed. In the third ℓ_* range, $k = 0$, 1, 2 states are observed, and so on. It must however be noted that excited states with $k \geq 1$ are radially unstable [111].

In the present paper and in the online repository [82] we focus on ℓ/μ ratios up to $(\ell/\mu)^2 = 20$, for which scalarized black holes with $\bar{\varphi} = 0$ have $\varphi_H \approx \pm 0.70$. This translates into $\ell_*^2 \lesssim 4.59$ using Eq. (25). For such ℓ_* values, Ref. [111,112] showed that only ground states exist, hence the presence of at most one pair of nonzero sensitivities α at $\bar{\varphi} = 0$ in Fig. 6. Moreover Refs. [111,112] proved that ground states are always radially and axially stable, when $\bar{\varphi} = 0$ if $\ell_*^2 \lesssim 25.02$. This implies that our scalarized black holes are stable at least when $\bar{\varphi} = 0$.

Fig. 12 shows $\log_{10}|\bar{\varphi}|$ as a function of φ_H (top panel) and the regularity condition (12) (bottom panel) for $\ell_*^2 = \{0.7, 1.0, 1.56, 2.78, 4.58\}$. The smallest ℓ_* values are respectively slightly below the scalarization threshold $\ell_*^2 \approx 0.725$, while the other values are those of Table I.

[1] B. P. Abbott *et al.* (LIGO Scientific, Virgo Collaborations), GWTC-1: A Gravitational-Wave Transient Catalog of Compact Binary Mergers Observed by LIGO and Virgo during the First and Second Observing Runs, Phys. Rev. X **9**, 031040 (2019).

[2] R. Abbott *et al.* (LIGO Scientific, Virgo Collaborations), GWTC-2: Compact Binary Coalescences Observed by LIGO and Virgo During the First Half of the Third Observing Run, Phys. Rev. X **11**, 021053 (2021).

[3] R. Abbott *et al.* (LIGO Scientific, VIRGO, KAGRA Collaborations), GWTC-3: Compact binary coalescences observed by LIGO and Virgo during the second part of the third observing run, arXiv:2111.03606.

[4] B. P. Abbott *et al.* (LIGO Scientific, Virgo Collaborations), Tests of General Relativity with GW150914, Phys. Rev. Lett. **116**, 221101 (2016); **121**, 129902(E) (2018).

[5] N. Yunes, K. Yagi, and F. Pretorius, Theoretical physics implications of the binary black-hole mergers GW150914 and GW151226, Phys. Rev. D **94**, 084002 (2016).

[6] B. P. Abbott *et al.* (LIGO Scientific, Virgo Collaborations), Tests of general relativity with the binary black hole signals from the LIGO-Virgo catalog GWTC-1, Phys. Rev. D **100**, 104036 (2019).

[7] R. Abbott *et al.* (LIGO Scientific, Virgo Collaborations), Tests of general relativity with binary black holes from the second LIGO-Virgo gravitational-wave transient catalog, Phys. Rev. D **103**, 122002 (2021).

[8] R. Abbott *et al.* (LIGO Scientific, VIRGO, KAGRA Collaborations), Tests of general relativity with GWTC-3, arXiv:2112.06861.

[9] A. Ghosh, R. Brito, and A. Buonanno, Constraints on quasinormal-mode frequencies with LIGO-Virgo binary–black-hole observations, Phys. Rev. D **103**, 124041 (2021).

[10] R. Nair, S. Perkins, H. O. Silva, and N. Yunes, Fundamental Physics Implications for Higher-Curvature Theories from Binary Black Hole Signals in the LIGO-Virgo Catalog GWTC-1, Phys. Rev. Lett. **123**, 191101 (2019).

[11] S. E. Perkins, R. Nair, H. O. Silva, and N. Yunes, Improved gravitational-wave constraints on higher-order curvature theories of gravity, Phys. Rev. D **104**, 024060 (2021).

[12] Z. Lyu, N. Jiang, and K. Yagi, Constraints on Einstein-dilation-Gauss-Bonnet gravity from black hole-neutron star gravitational wave events, Phys. Rev. D **105**, 064001 (2022).

[13] E. Berti *et al.*, Testing general relativity with present and future astrophysical observations, Classical Quantum Gravity **32**, 243001 (2015).

[14] E. Berti, K. Yagi, and N. Yunes, Extreme gravity tests with gravitational waves from compact binary coalescences: (I) Inspiral-merger, Gen. Relativ. Gravit. **50**, 46 (2018).

[15] E. Berti, K. Yagi, H. Yang, and N. Yunes, Extreme gravity tests with gravitational waves from compact binary coalescences: (II) Ringdown, Gen. Relativ. Gravit. **50**, 49 (2018).

[16] R. R. Metsaev and A. A. Tseytlin, Order α' (two loop) equivalence of the string equations of motion and the sigma model weyl invariance conditions: Dependence on the dilaton and the antisymmetric tensor, Nucl. Phys. **B293**, 385 (1987).

[17] C. Charmousis, From Lovelock to Horndeski's generalized scalar-tensor theory, Lect. Notes Phys. **892**, 25 (2015).

[18] T. Kobayashi, M. Yamaguchi, and J. Yokoyama, Generalized G-inflation: Inflation with the most general second-order field equations, Prog. Theor. Phys. **126**, 511 (2011).

[19] T. Kobayashi, Horndeski theory and beyond: A review, Rep. Prog. Phys. **82**, 086901 (2019).

[20] K. Yagi, L. C. Stein, and N. Yunes, Challenging the presence of scalar charge and dipolar radiation in binary pulsars, Phys. Rev. D **93**, 024010 (2016).

[21] P. A. Cano and A. Ruipérez, Leading higher-derivative corrections to Kerr geometry, J. High Energy Phys. 05 (2019) 189; 03 (2020) 187.

[22] S. Mignemi and N. R. Stewart, Charged black holes in effective string theory, Phys. Rev. D **47**, 5259 (1993).

[23] P. Kanti, N. E. Mavromatos, J. Rizos, K. Tamvakis, and E. Winstanley, Dilatonic black holes in higher curvature string gravity, Phys. Rev. D **54**, 5049 (1996).

[24] Z.-K. Guo, N. Ohta, and T. Torii, Black holes in the dilatonic Einstein-Gauss-Bonnet theory in various dimensions. I. Asymptotically flat black holes, Prog. Theor. Phys. **120**, 581 (2008).

[25] P. Pani and V. Cardoso, Are black holes in alternative theories serious astrophysical candidates? The Case for Einstein-Dilaton-Gauss-Bonnet black holes, Phys. Rev. D **79**, 084031 (2009).
[26] N. Yunes and L. C. Stein, Nonspinning black holes in alternative theories of gravity, Phys. Rev. D **83**, 104002 (2011).
[27] P. Pani, C. F. B. Macedo, L. C. B. Crispino, and V. Cardoso, Slowly rotating black holes in alternative theories of gravity, Phys. Rev. D **84**, 087501 (2011).
[28] T. P. Sotiriou and S.-Y. Zhou, Black Hole Hair in Generalized Scalar-Tensor Gravity, Phys. Rev. Lett. **112**, 251102 (2014).
[29] T. P. Sotiriou and S.-Y. Zhou, Black hole hair in generalized scalar-tensor gravity: An explicit example, Phys. Rev. D **90**, 124063 (2014).
[30] A. Maselli, H. O. Silva, M. Minamitsuji, and E. Berti, Slowly rotating black hole solutions in Horndeski gravity, Phys. Rev. D **92**, 104049 (2015).
[31] B. Kleihaus, J. Kunz, S. Mojica, and E. Radu, Spinning black holes in Einstein–Gauss-Bonnet–dilaton theory: Nonperturbative solutions, Phys. Rev. D **93**, 044047 (2016).
[32] G. Antoniou, A. Bakopoulos, and P. Kanti, Evasion of No-Hair Theorems and Novel Black-Hole Solutions in Gauss-Bonnet Theories, Phys. Rev. Lett. **120**, 131102 (2018).
[33] K. Prabhu and L. C. Stein, Black hole scalar charge from a topological horizon integral in Einstein-dilaton-Gauss-Bonnet gravity, Phys. Rev. D **98**, 021503 (2018).
[34] M. Saravani and T. P. Sotiriou, Classification of shift-symmetric Horndeski theories and hairy black holes, Phys. Rev. D **99**, 124004 (2019).
[35] A. Sullivan, N. Yunes, and T. P. Sotiriou, Numerical black hole solutions in modified gravity theories: Spherical symmetry case, Phys. Rev. D **101**, 044024 (2020).
[36] A. Sullivan, N. Yunes, and T. P. Sotiriou, Numerical black hole solutions in modified gravity theories: Axial symmetry case, Phys. Rev. D **103**, 124058 (2021).
[37] J. F. M. Delgado, C. A. R. Herdeiro, and E. Radu, Spinning black holes in shift-symmetric Horndeski theory, J. High Energy Phys. 04 (2020) 180.
[38] D. D. Doneva and S. S. Yazadjiev, New Gauss-Bonnet Black Holes with Curvature-Induced Scalarization in Extended Scalar-Tensor Theories, Phys. Rev. Lett. **120**, 131103 (2018).
[39] H. O. Silva, J. Sakstein, L. Gualtieri, T. P. Sotiriou, and E. Berti, Spontaneous Scalarization of Black Holes and Compact Stars from a Gauss-Bonnet Coupling, Phys. Rev. Lett. **120**, 131104 (2018).
[40] A. Dima, E. Barausse, N. Franchini, and T. P. Sotiriou, Spin-Induced Black Hole Spontaneous Scalarization, Phys. Rev. Lett. **125**, 231101 (2020).
[41] C. A. R. Herdeiro, E. Radu, H. O. Silva, T. P. Sotiriou, and N. Yunes, Spin-Induced Scalarized Black Holes, Phys. Rev. Lett. **126**, 011103 (2021).
[42] E. Berti, L. G. Collodel, B. Kleihaus, and J. Kunz, Spin-Induced Black-Hole Scalarization in Einstein-Scalar-Gauss-Bonnet Theory, Phys. Rev. Lett. **126**, 011104 (2021).
[43] K. Yagi, L. C. Stein, N. Yunes, and T. Tanaka, Post-Newtonian, quasi-circular binary inspirals in quadratic modified gravity, Phys. Rev. D **85**, 064022 (2012); **93**, 029902(E) (2016).
[44] L. C. Stein and K. Yagi, Parametrizing and constraining scalar corrections to general relativity, Phys. Rev. D **89**, 044026 (2014).
[45] S. E. Perkins, N. Yunes, and E. Berti, Probing fundamental physics with gravitational waves: The next generation, Phys. Rev. D **103**, 044024 (2021).
[46] A. Maselli, N. Franchini, L. Gualtieri, and T. P. Sotiriou, Detecting Scalar Fields with Extreme Mass Ratio Inspirals, Phys. Rev. Lett. **125**, 141101 (2020).
[47] F.-L. Julié and E. Berti, Post-Newtonian dynamics and black hole thermodynamics in Einstein-scalar-Gauss-Bonnet gravity, Phys. Rev. D **100**, 104061 (2019).
[48] B. Shiralilou, T. Hinderer, S. Nissanke, N. Ortiz, and H. Witek, Nonlinear curvature effects in gravitational waves from inspiralling black hole binaries, Phys. Rev. D **103**, L121503 (2021).
[49] B. Shiralilou, T. Hinderer, S. M. Nissanke, N. Ortiz, and H. Witek, Post-Newtonian gravitational and scalar waves in scalar-Gauss–Bonnet gravity, Classical Quantum Gravity **39**, 035002 (2022).
[50] L. Bernard, L. Blanchet, and D. Trestini, Gravitational waves in scalar-tensor theory to one-and-a-half post-Newtonian order, arXiv:2201.10924.
[51] H. Witek, L. Gualtieri, P. Pani, and T. P. Sotiriou, Black holes and binary mergers in scalar Gauss-Bonnet gravity: Scalar field dynamics, Phys. Rev. D **99**, 064035 (2019).
[52] J. L. Ripley and F. Pretorius, Hyperbolicity in spherical gravitational collapse in a Horndeski theory, Phys. Rev. D **99**, 084014 (2019).
[53] J. L. Ripley and F. Pretorius, Gravitational collapse in Einstein dilaton-Gauss–Bonnet gravity, Classical Quantum Gravity **36**, 134001 (2019).
[54] J. L. Ripley and F. Pretorius, Scalarized black hole dynamics in Einstein dilaton Gauss-Bonnet gravity, Phys. Rev. D **101**, 044015 (2020).
[55] M. Okounkova, Numerical relativity simulation of GW150914 in Einstein dilaton Gauss-Bonnet gravity, Phys. Rev. D **102**, 084046 (2020).
[56] W. E. East and J. L. Ripley, Evolution of Einstein-scalar-Gauss-Bonnet gravity using a modified harmonic formulation, Phys. Rev. D **103**, 044040 (2021).
[57] H. O. Silva, H. Witek, M. Elley, and N. Yunes, Dynamical Descalarization in Binary Black Hole Mergers, Phys. Rev. Lett. **127**, 031101 (2021).
[58] W. E. East and J. L. Ripley, Dynamics of Spontaneous Black Hole Scalarization and Mergers in Einstein-Scalar-Gauss-Bonnet Gravity, Phys. Rev. Lett. **127**, 101102 (2021).
[59] H.-J. Kuan, D. D. Doneva, and S. S. Yazadjiev, Dynamical Formation of Scalarized Black Holes and Neutron Stars through Stellar Core Collapse, Phys. Rev. Lett. **127**, 161103 (2021).
[60] G. Papallo and H. S. Reall, On the local well-posedness of Lovelock and Horndeski theories, Phys. Rev. D **96**, 044019 (2017).

[61] A. D. Kovács and H. S. Reall, Well-posed formulation of Lovelock and Horndeski theories, Phys. Rev. D **101**, 124003 (2020).
[62] A. D. Kovács and H. S. Reall, Well-Posed Formulation of Scalar-Tensor Effective Field Theory, Phys. Rev. Lett. **124**, 221101 (2020).
[63] F.-L. Julié and E. Berti, $d+1$ formalism in Einstein-scalar-Gauss-Bonnet gravity, Phys. Rev. D **101**, 124045 (2020).
[64] H. Witek, L. Gualtieri, and P. Pani, Towards numerical relativity in scalar Gauss-Bonnet gravity: $3+1$ decomposition beyond the small-coupling limit, Phys. Rev. D **101**, 124055 (2020).
[65] A. D. Kovács, On the construction of asymptotically flat initial data in scalar-tensor effective field theory, arXiv:2103.06895.
[66] D. M. Eardley, Observable effects of a scalar gravitational field in a binary pulsar, Astrophys. J. **196**, L59 (1975).
[67] C. M. Will and H. W. Zaglauer, Gravitational radiation, close binary systems, and the Brans-Dicke theory of gravity, Astrophys. J. **346**, 366 (1989).
[68] T. Damour and G. Esposito-Farèse, Tensor multiscalar theories of gravitation, Classical Quantum Gravity **9**, 2093 (1992).
[69] T. Damour and G. Esposito-Farèse, Testing gravity to second post-Newtonian order: A field theory approach, Phys. Rev. D **53**, 5541 (1996).
[70] T. Damour and G. Esposito-Farèse, Tensor-scalar gravity and binary pulsar experiments, Phys. Rev. D **54**, 1474 (1996).
[71] F.-L. Julié, On the motion of hairy black holes in Einstein-Maxwell-dilaton theories, J. Cosmol. Astropart. Phys. 01 (2018) 026.
[72] M. Khalil, N. Sennett, J. Steinhoff, J. Vines, and A. Buonanno, Hairy binary black holes in Einstein-Maxwell-dilaton theory and their effective-one-body description, Phys. Rev. D **98**, 104010 (2018).
[73] F.-L. Julié, Gravitational radiation from compact binary systems in Einstein-Maxwell-dilaton theories, J. Cosmol. Astropart. Phys. 10 (2018) 033.
[74] K. Yagi, D. Blas, E. Barausse, and N. Yunes, Constraints on Einstein-Æther theory and Hořava gravity from binary pulsar observations, Phys. Rev. D **89**, 084067 (2014); **90**, 069902(E) (2014); **90**, 069901(E) (2014).
[75] T. Gupta, M. Herrero-Valea, D. Blas, E. Barausse, N. Cornish, K. Yagi, and N. Yunes, New binary pulsar constraints on Einstein-Æther theory after GW170817, Classical Quantum Gravity **38**, 195003 (2021).
[76] N. Deruelle, J. Katz, and S. Ogushi, Conserved charges in Einstein Gauss-Bonnet theory, Classical Quantum Gravity **21**, 1971 (2004).
[77] S. C. Davis, Generalized Israel junction conditions for a Gauss-Bonnet brane world, Phys. Rev. D **67**, 024030 (2003).
[78] R. C. Myers, Higher derivative gravity, surface terms and string theory, Phys. Rev. D **36**, 392 (1987).
[79] C. W. Misner and D. H. Sharp, Relativistic equations for adiabatic, spherically symmetric gravitational collapse, Phys. Rev. **136**, B571 (1964).
[80] S. R. Coleman, J. Preskill, and F. Wilczek, Quantum hair on black holes, Nucl. Phys. **B378**, 175 (1992).
[81] A. H. K. R., E. R. Most, J. Noronha, H. Witek, and N. Yunes, How do spherical black holes grow monopole hair?, Phys. Rev. D **105**, 064041 (2022).
[82] F.-L. Julié and H. O. Silva, Black hole sensitivities in Einstein-scalar-Gauss-Bonnet gravity (2022), https://bitbucket.org/hosilva/bh_sensititivities_esgb.
[83] M. Cárdenas, F.-L. Julié, and N. Deruelle, Thermodynamics sheds light on black hole dynamics, Phys. Rev. D **97**, 124021 (2018).
[84] R. M. Wald, Black hole entropy is the Noether charge, Phys. Rev. D **48**, R3427 (1993).
[85] V. Iyer and R. M. Wald, Some properties of Noether charge and a proposal for dynamical black hole entropy, Phys. Rev. D **50**, 846 (1994).
[86] T. Torii, H. Yajima, and K.-i. Maeda, Dilatonic black holes with Gauss-Bonnet term, Phys. Rev. D **55**, 739 (1997).
[87] D. Christodoulou, Reversible and Irreversible Transforations in Black Hole Physics, Phys. Rev. Lett. **25**, 1596 (1970).
[88] W. H. Press, S. A. Teukolsky, W. T. Vetterling, and B. P. Flannery, *Numerical Recipes in C++: The Art of Scientific Computing* (Cambridge University Press, Cambridge, 2002).
[89] H. O. Silva, C. F. B. Macedo, T. P. Sotiriou, L. Gualtieri, J. Sakstein, and E. Berti, Stability of scalarized black hole solutions in scalar-Gauss-Bonnet gravity, Phys. Rev. D **99**, 064011 (2019).
[90] C. F. B. Macedo, J. Sakstein, E. Berti, L. Gualtieri, H. O. Silva, and T. P. Sotiriou, Self-interactions and spontaneous black hole scalarization, Phys. Rev. D **99**, 104041 (2019).
[91] T. Anson, E. Babichev, C. Charmousis, and S. Ramazanov, Cosmological instability of scalar-Gauss-Bonnet theories exhibiting scalarization, J. Cosmol. Astropart. Phys. 06 (2019) 023.
[92] A. Buonanno and T. Damour, Effective one-body approach to general relativistic two-body dynamics, Phys. Rev. D **59**, 084006 (1999).
[93] A. Buonanno and T. Damour, Transition from inspiral to plunge in binary black hole coalescences, Phys. Rev. D **62**, 064015 (2000).
[94] F.-L. Julié and N. Deruelle, Two-body problem in scalar-tensor theories as a deformation of general relativity: An effective-one-body approach, Phys. Rev. D **95**, 124054 (2017).
[95] F.-L. Julié, Reducing the two-body problem in scalar-tensor theories to the motion of a test particle: A scalar-tensor effective-one-body approach, Phys. Rev. D **97**, 024047 (2018).
[96] P. Kanti, B. Kleihaus, and J. Kunz, Stable Lorentzian wormholes in dilatonic Einstein-Gauss-Bonnet theory, Phys. Rev. D **85**, 044007 (2012).
[97] L. Bernard, Dynamics of compact binary systems in scalar-tensor theories: Equations of motion to the third post-Newtonian order, Phys. Rev. D **98**, 044004 (2018).
[98] L. Bernard, Dynamics of compact binary systems in scalar-tensor theories: II. Center-of-mass and conserved quantities to 3PN order, Phys. Rev. D **99**, 044047 (2019).
[99] M. Khalil, N. Sennett, J. Steinhoff, and A. Buonanno, Theory-agnostic framework for dynamical scalarization of compact binaries, Phys. Rev. D **100**, 124013 (2019).

[100] E. Barausse, C. Palenzuela, M. Ponce, and L. Lehner, Neutron-star mergers in scalar-tensor theories of gravity, Phys. Rev. D **87**, 081506 (2013).
[101] C. Palenzuela, E. Barausse, M. Ponce, and L. Lehner, Dynamical scalarization of neutron stars in scalar-tensor gravity theories, Phys. Rev. D **89**, 044024 (2014).
[102] M. Shibata, K. Taniguchi, H. Okawa, and A. Buonanno, Coalescence of binary neutron stars in a scalar-tensor theory of gravity, Phys. Rev. D **89**, 084005 (2014).
[103] K. Taniguchi, M. Shibata, and A. Buonanno, Quasiequilibrium sequences of binary neutron stars undergoing dynamical scalarization, Phys. Rev. D **91**, 024033 (2015).
[104] N. Sennett and A. Buonanno, Modeling dynamical scalarization with a resummed post-Newtonian expansion, Phys. Rev. D **93**, 124004 (2016).
[105] N. Sennett, L. Shao, and J. Steinhoff, Effective action model of dynamically scalarizing binary neutron stars, Phys. Rev. D **96**, 084019 (2017).
[106] T. Damour and G. Esposito-Farèse, Nonperturbative Strong Field Effects in Tensor-Scalar Theories of Gravitation, Phys. Rev. Lett. **70**, 2220 (1993).
[107] G. Antoniou, L. Bordin, and T. P. Sotiriou, Compact object scalarization with general relativity as a cosmic attractor, Phys. Rev. D **103**, 024012 (2021).
[108] G. Ventagli, A. Lehébel, and T. P. Sotiriou, Onset of spontaneous scalarization in generalized scalar-tensor theories, Phys. Rev. D **102**, 024050 (2020).
[109] G. Antoniou, A. Lehébel, G. Ventagli, and T. P. Sotiriou, Black hole scalarization with Gauss-Bonnet and Ricci scalar couplings, Phys. Rev. D **104**, 044002 (2021).
[110] D. D. Doneva, K. V. Staykov, S. S. Yazadjiev, and R. Z. Zheleva, Multiscalar Gauss-Bonnet gravity: Hairy black holes and scalarization, Phys. Rev. D **102**, 064042 (2020).
[111] J. L. Blázquez-Salcedo, D. D. Doneva, J. Kunz, and S. S. Yazadjiev, Radial perturbations of the scalarized Einstein-Gauss-Bonnet black holes, Phys. Rev. D **98**, 084011 (2018).
[112] J. L. Blázquez-Salcedo, D. D. Doneva, S. Kahlen, J. Kunz, P. Nedkova, and S. S. Yazadjiev, Axial perturbations of the scalarized Einstein-Gauss-Bonnet black holes, Phys. Rev. D **101**, 104006 (2020).
[113] J. L. Blázquez-Salcedo, D. D. Doneva, S. Kahlen, J. Kunz, P. Nedkova, and S. S. Yazadjiev, Polar quasinormal modes of the scalarized Einstein-Gauss-Bonnet black holes, Phys. Rev. D **102**, 024086 (2020).
[114] J. D. Hunter, Matplotlib: A 2D graphics environment, Comput. Sci. Eng. **9**, 90 (2007).
[115] T. Tantau, The TikZ and PGF Packages, https://github.com/pgf-tikz/pgf.